

NONLINEAR OPTICAL PHENOMENA IN SILICON NANOWAVEGUIDES
FOR THE MID-INFRARED WAVELENGTH REGION

A Dissertation

Presented to the Faculty of the Graduate School
of Cornell University

In Partial Fulfillment of the Requirements for the Degree of
Doctor of Philosophy

by

Ryan Kin Wah Lau

May 2015

© 2015 Ryan Kin Wah Lau

NONLINEAR OPTICAL PHENOMENA IN SILICON NANOWAVEGUIDES
FOR THE MID-INFRARED WAVELENGTH REGION

Ryan Kin Wah Lau, Ph. D.

Cornell University 2015

Silicon photonics has shown great promise as an integrated solution for efficient nonlinear optical interactions in compact, chip-scale devices. While there has been much work over the past decade on developing a variety of all-optical devices for telecom applications, an emerging area of research focuses on extending the operational wavelength of such devices to the mid-infrared (MIR) regime. By leveraging enhanced nonlinear optical effects and exploiting reduced losses at longer wavelengths, silicon photonic technology may be extended into a new realm of applications at MIR wavelengths.

In this thesis we investigate nonlinear optical phenomena in silicon nanowaveguides for the MIR wavelength region. We present a numerical analysis of broadband four-wave mixing (FWM) and supercontinuum generation (SCG) in silicon nanowaveguides in the 2- μm region. We demonstrate for the first time continuous-wave FWM-based wavelength conversion between the telecom and MIR wavelength ranges. We also demonstrate the first silicon-based, octave-spanning supercontinuum (SCG) as well as the longest wavelength generated via SCG on a silicon chip. Next we numerically investigate silicon microresonator-based optical frequency combs using a modified Lugiato-Lefever model and discuss the implications of nonlinear loss effects, identifying regimes in the MIR in which broadband parametric oscillation may be achieved. While much of this work focuses on the silicon-on-insulator (SOI) platform

and silicon dioxide or air claddings, we also introduce a novel waveguiding platform for wavelengths beyond 3 μm . We design and fabricate devices using standard SOI wafers with a top cladding of silicon nitride and demonstrate broadband FWM near 2 μm .

BIOGRAPHICAL SKETCH

Ryan Lau was born on April 16, 1986 in sunny Honolulu, Hawaii, but has studied in the sub-zero winters of Boston and Ithaca, a relocation that his friends still think ridiculous. From a young age, it was suggested that he become a doctor, but after fainting each time he had blood drawn, that life path was quickly abandoned. He attended Iolani School for middle school and high school, where he developed a lifelong passion for mathematics, science, and obscure nerd-related humor. Along the way, he met many inspiring teachers and wonderful friends who had a profound impact in shaping his adolescent years. He graduated as a valedictorian for the Class of 2004 and then matriculated to Boston University. In 2007, he graduated Summa Cum Laude with a Bachelors of Science in Electrical and Computer Engineering. Fascinated by the prospect of being paid to learn, Ryan decided to pursue a doctorate at Cornell University in Professor Alexander Gaeta's research group in the field of nonlinear optics. He explored the boundaries of physics by playing with lasers, finally culminating in a doctorate degree in Electrical and Computer Engineering in January 2015.

ACKNOWLEDGMENTS

First and foremost, I would like to thank my advisor Professor Alexander Gaeta for his invaluable guidance and mentorship during my graduate career at Cornell. His commitment to and success in working on challenging problems at the forefront of scientific research play a large role in attracting researchers to his lab, but I am truly appreciative of the collegial and collaborative atmosphere that he has fostered within his group. In addition, I would also like to thank my committee members Professor Michal Lipson and Professor Farhan Rana for their insight and discussion which have been helpful in guiding this research.

Much of the success of this work would simply not be possible without the brilliant work and support of my colleagues, and I would like to acknowledge and thank the following people specifically: Dr. Michaël Ménard and Austin Griffith, for their hours and hours (and hours) spent fabricating devices in the clean room. Their meticulous fabrication skills have led to devices with unprecedented performance, enabling many of the record-breaking results presented here. Dr. Michael Lamont, for his assistance in developing a significant portion of the experimental procedures and numerical analyses used here, and for enlightening me with his experiences and insight during our many coffee chats and ~~gaming~~ brainstorming sessions. Dr. Yoshitomo Okawachi, for an infinite amount of stimulating discussions and research ideas, and for his hospitality in welcoming me into his home whenever he found an excuse. Dr. Reza Salem, for providing direction in experimental and analytical techniques, which I especially found useful during my early years. Dr. Bonggu Shim, for generously giving his time and unparalleled technical prowess to resuscitate downed laser systems, and for never running out of high fives or spontaneous dance moves.

I came to Ithaca expecting a great place for study, but I did not anticipate the close friendships that would form along the way. Nicholas Wildman, roommate-turned-best-man-turned-DJ-extraordinaire, was a constant source of unpredictable experiences and unforgettable antics, who added a touch of much appreciated randomness and mild fun to every evening. To my dinner groups, gamer geeks, card hustlers, and drinking buddies, and to the members of the Gaeta Lab, both official and honorary, thank you for your warm personalities and good company over the years. I will miss you all.

Above all, I would like to thank my family for their love, support, and constant reminders of how long I've been in graduate school. My beautiful wife, Xi Yan, has been brightening my days with her energetic personality from the moment we met, and my brother Roger has traveled across countries and oceans many times to join me in support throughout my life. I will be forever grateful to my parents, Ronnie and Kit Mei Lau, for their work and sacrifice to provide me with the best education possible. They were my very first teachers and role models, and have instilled in me a passion for curiosity and learning. Thank you, Mom and Dad.

TABLE OF CONTENTS

| | |
|---|-----------|
| Biographical Sketch | iii |
| Acknowledgements | iv |
| Table of Contents | vi |
| List of Abbreviations | vii |
| 1 Introduction | 1 |
| 1.1 Silicon photonics | 1 |
| 1.2 Nonlinear optics in silicon nanowaveguides | 3 |
| 1.3 Silicon in the mid-infrared regime | 6 |
| 1.4 Thesis layout | 9 |
| 2 Numerical and experimental techniques | 17 |
| 2.1 Nonlinear Schrödinger equation | 17 |
| 2.2 Split-step Fourier method | 18 |
| 2.3 Experimental techniques | 19 |
| 3 Continuous-wave four-wave mixing in the mid-infrared region | 22 |
| 3.1 Energy conservation and phase matching | 23 |
| 3.2 Numerical modeling of four-wave mixing process | 24 |
| 3.3 Nanowaveguide design and fabrication | 25 |
| 3.4 Experimental demonstration of wavelength conversion | 27 |
| 3.5 Summary | 32 |
| 4 Mid-infrared supercontinuum generation | 35 |
| 4.1 Numerical modeling of supercontinuum generation dynamics | 36 |
| 4.2 Experimental demonstration of supercontinuum generation | 39 |
| 4.3 Three-photon absorption and free-carrier effects from low- and high-repetition-rate sources | 41 |
| 4.4 Summary | 44 |
| 5 Microresonator-based parametric comb generation | 48 |
| 5.1 Modified Lugiato-Lefever model | 49 |
| 5.2 Parametric oscillation in telecom and mid-infrared regimes | 52 |
| 5.3 Summary | 58 |
| 6 Silicon-nitride-clad nanowaveguides | 63 |
| 6.1 Nanowaveguide design, fabrication, and characterization | 63 |
| 6.2 Four-wave mixing at mid-infrared wavelengths | 66 |
| 6.3 Summary | 67 |
| 7 Future Directions | 69 |

LIST OF ABBREVIATIONS

| | |
|--------------------------------|---|
| 2PA | Two-Photon Absorption |
| 3PA | Three-Photon Absorption |
| 4PA | Four-Photon Absorption |
| CMOS | Complementary Metal-Oxide-Semiconductor |
| CW | Continuous Wave |
| FCA | Free-Carrier Absorption |
| FCD | Free-Carrier Dispersion |
| FTIR | Fourier-Transform Infrared Spectrometer |
| FWM | Four-Wave Mixing |
| GVD | Group-Velocity Dispersion |
| LL | Lugiato Leferver |
| MIR | Mid-Infrared |
| NIR | Near-Infrared |
| NLSE | Nonlinear Schrödinger Equation |
| OFC | Optical Frequency Comb |
| OPO | Optical Parametric Oscillator |
| PECVD | Plasma-Enhanced Chemical Vapor Deposition |
| SCG | Supercontinuum Generation |
| SOI | Silicon-on-Insulator |
| Si ₃ N ₄ | Silicon Nitride |
| SiO ₂ | Silicon Dioxide |
| TE | Transverse Electric |

CHAPTER 1

INTRODUCTION

Photonics, the science of light, describes the generation and manipulation of photons, and is poised to play a key role in the advancement of next-generation technologies. With the invention of the laser in 1960 [1] and the subsequent realization of low-loss optical fibers [2, 3], the field of photonics has yielded impressive advances in optical communication systems and has given rise to our modern-day information technology revolution. While photonics has traditionally referred to the manipulation of light for use in telecommunications, the field has since expanded to encompass a wide range of applications, including computing, security, sensing, manufacturing, and medicine. Inspired by achievements in microelectronic integrated circuits, integrated optics has been proposed as a solution for on-chip integration of high-bandwidth optical components, such as lasers, modulators, and filters [4]. This large-scale consolidation of multiple optical components onto a single monolithic device would enable reductions in packaging complexity, cost, size, and power consumption.

1.1 Silicon photonics

Early efforts to develop a practical integrated photonic platform have focused on direct bandgap semiconductors such as gallium arsenide [5] and indium phosphide [5, 6]. Silicon has been traditionally thought to be a poor photonic material due to its indirect bandgap, which poses limitations for active optoelectronic functionality such as light emission and optical amplification. More recently, however, Raman lasing [7] and four-wave mixing-based parametric gain [8] have been demonstrated in silicon, making it an extremely promising material candidate for integrated photonics.

Over the past decade, significant progress has been made to advance silicon as the photonic platform of choice [9-13], since this technology would be able to leverage the mature and large-scale manufacturing base of existing complementary metal-oxide-semiconductor (CMOS) fabrication processes. Due to the high refractive index of silicon ($n \sim 3.5$), optical waveguides exhibit a large refractive index contrast between the silicon core and silicon dioxide (SiO_2) cladding, enabling strong confinement of the optical mode and compact device footprints. This confinement introduces significant waveguide dispersion, allowing fine control of the nanowaveguide group-velocity dispersion (GVD) [14-16].

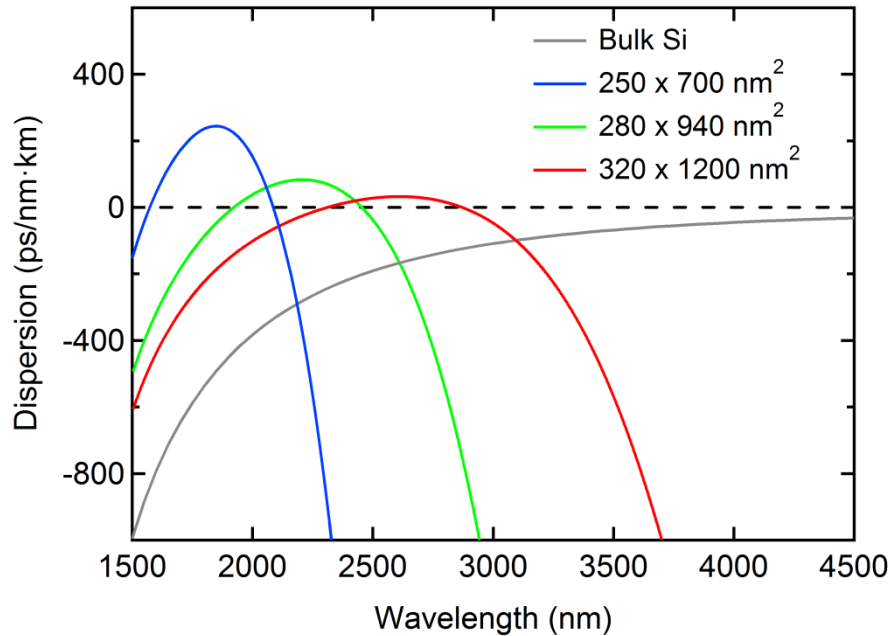


Figure 1.1: Simulated GVD for the TE mode of silicon nanowaveguides with a ranging of cross sections. GVD for bulk silicon is shown in grey.

Bulk silicon exhibits large, normal GVD at near-infrared (NIR) and mid-infrared (MIR) wavelengths, and although the GVD tends toward zero with increasing wavelength, it remains normal from 1.36 μm to 11 μm , the wavelength range

measured by Salzberg and Villa [17]. However, nanowaveguides with dimensions on the scale of the optical wavelength can introduce enough waveguide dispersion to compensate the intrinsic material dispersion of silicon and even result in regions of anomalous GVD (Fig. 1.1). Consequently, proper engineering of the nanowaveguide cross section can facilitate broadband nonlinear optical phenomena such as four-wave mixing (FWM) [8, 18-20], supercontinuum generation (SCG) [21, 22], and optical parametric oscillation [23-26]. An in-depth discussion on the role of dispersion for each of these processes will be presented in following chapters.

1.2 Nonlinear optics in silicon nanowaveguides

Nonlinear optical processes in silicon are governed by the third-order susceptibility $\chi^{(3)}$. The real and imaginary parts of $\chi^{(3)}$ give rise to the nonlinear index n_2 and the two-photon absorption (2PA) coefficient β_{2PA} . These processes are intensity-dependent, and can influence the refractive index n and absorption α of the material through the relations

$$n = n_0 + n_2 I, \quad (1.1)$$

$$\alpha = \alpha_0 + \beta_{2PA} I, \quad (1.2)$$

where n_0 and α_0 are the linear refractive index and absorption coefficient, respectively, n_2 is the nonlinear index, β_{2PA} is the 2PA coefficient, and I is the optical intensity. These nonlinear parameters have been experimentally measured and are presented in Fig. 1.2 [27-31].

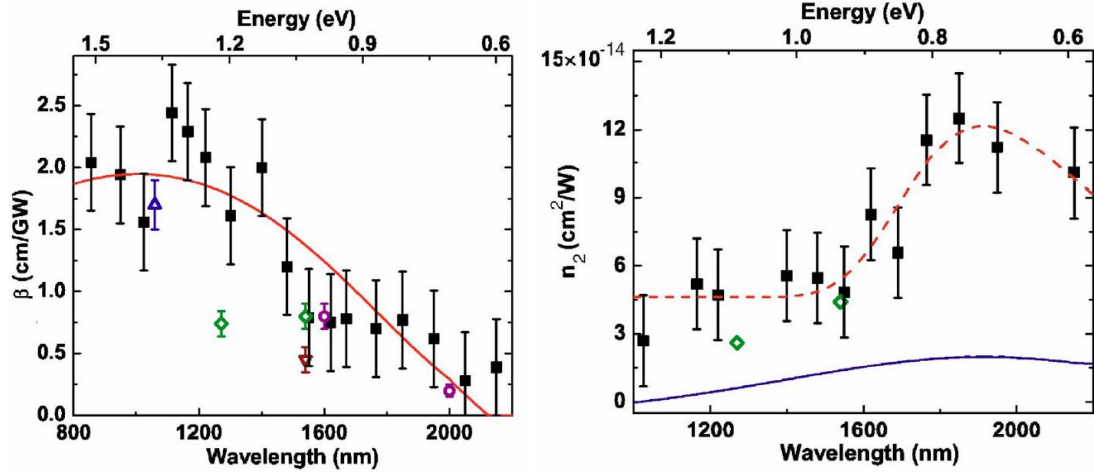


Figure 1.2: Measurements of 2PA coefficient β_{2PA} and nonlinear index n_2 for silicon. Figures taken from Bristow et al. [31].

The data show that the 2PA coefficient decreases with increasing wavelength beyond 1.2 μm and drops to zero for wavelengths beyond 2.2 μm , which corresponds to half of the bandgap energy of silicon. The solid red curve in Fig. 1.2 represents a best fit for the theoretical dispersion curve of the degenerate β_{2PA} based on calculations by Garcia and Kalyanaraman [32]. The calculations include “forbidden-forbidden,” “allowed-forbidden,” and “allowed-allowed” optical transitions, and the fit appears consistent with measured data after the inclusion of a scaling factor [31]. In addition, the data show that the nonlinear index exhibits a local maximum near 1.9 μm before decreasing at longer wavelengths. The dashed red curve in Fig 1.2 is a guide to the eye, and the solid blue curve is a theoretical estimate based on the Kramers-Krönig transformation of the nondegenerate β_{2PA} . This expression is given by [31]

$$n_2(\omega) = \frac{c}{\pi} \int \frac{\beta_{2PA}(\omega, \omega')}{\omega^2} - \omega'^2 d\omega' \quad (1.3)$$

with the approximation $\beta_{2PA}(\omega, \omega') = \beta_{2PA}((\omega + \omega')/2)$. Both the measured data and theoretical approximation peak near 1.9 μm , but have greatly differing values. The

authors attribute the discrepancy to the neglect of Raman and quadratic stark contributions in the Kramers-Krönig transform along with the simple approximation for the nondegenerate $\beta_{2PA}(\omega, \omega')$ [31].

The nonlinear index n_2 of silicon is $4 \times 10^{-14} \text{ cm}^2/\text{W}$ near telecom wavelengths [29, 31], which is approximately 200 times that of silica glass [19]. It is this large nonlinear index, in conjunction with the refractive index discussed in the previous section, which enables efficient nonlinear optical interactions in silicon at relatively low power levels [33-35]. To date, many nonlinear optical processes have been demonstrated in silicon nanowaveguides, including self-phase modulation (SPM) [36-38], cross-phase modulation (XPM) [39-41], FWM [8, 42-49], SCG [50], and stimulated Raman scattering (SRS) [7, 51-54]. Since these devices have been designed for the NIR wavelength regime around $1.55 \mu\text{m}$, they are fundamentally limited by the presence of 2PA and the resulting free carriers.

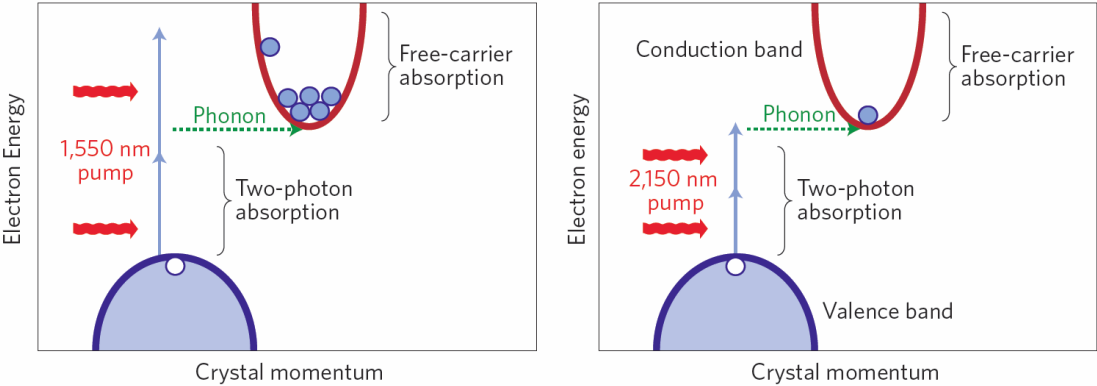


Figure 1.3: Schematic of TPA process in silicon leading to generation of free carriers for NIR and MIR pumps. Figures taken from Jalali [55].

2PA is a nonlinear process in which two photons are absorbed to excite an electron from the valence band to the conduction band (Fig. 1.3). The generated free

carriers can then cause additional loss through free-carrier absorption (FCA) and can also change the refractive index through free-carrier dispersion (FCD). At high intensities, a population of free carriers can accumulate, resulting in significant optical loss. While 2PA and free-carrier effects have been leveraged to realize all-optical signal processing functionalities [56-59], these effects are generally detrimental to the majority of nonlinear optical processes [18, 36, 37, 50, 60-63].

1.3 Silicon in the mid-infrared regime

Though much of the rapid progress of silicon photonics has occurred at telecom wavelengths, the inherent advantages of material transparency and high nonlinearity are still present at longer MIR wavelengths (Fig. 1.4) [64, 65]. Consequently, there has recently been great interest in leveraging this technology for MIR applications. In this thesis we focus on the 2 – 5 μm wavelength range. The motivation is twofold; on-chip integration with well-developed telecom components and improved efficiency due to reduced nonlinear losses.

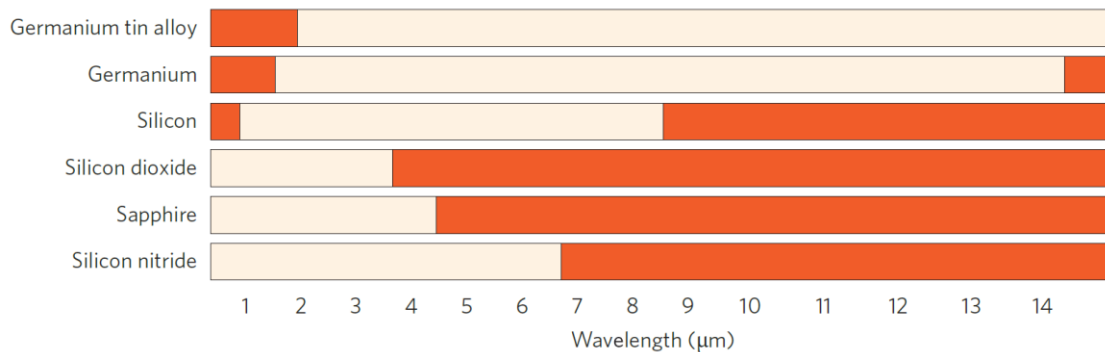


Figure 1.4: Regions of optical transparency for typical waveguide core materials. White regions correspond to wavelength ranges over which propagation loss is less than 2 dB/cm. Figure taken from Soref [65].

Currently, there are few commercially available monolithic sources and detectors which work well at room temperature over the 2 – 5 μm wavelength range. There have been several promising research efforts to develop MIR sources, including quantum cascade lasers [66, 67], fiber lasers [68-70], solid-state lasers (e.g., Cr^{2+} -doped lasers) [71, 72], and nonlinear wavelength conversion of mode-locked lasers [73-75]. In addition, waveguiding architectures such as silicon-on-sapphire [76, 77] and germanium-on-silicon [78] have already been realized. In light of these recent developments, it is clear that on-chip integration of active and passive devices for the MIR region using silicon-on-insulator (SOI) technology would enable a level of performance, compactness, and robustness not readily obtainable.

An additional benefit arises from the reduced 2PA in silicon at MIR wavelengths beyond $\lambda = 2.2 \mu\text{m}$ (Fig. 1.2). Furthermore, the generation rate of free carriers is significantly reduced due to the lower number of available electron states (Fig. 1.3), and thus FCA is mitigated as well. The nonlinear figure of merit (FOM) is defined as $FOM = n_2/(\lambda\beta_{2PA})$, and several values over different wavelength regions are given in Table 1.1. There is clear improvement by nearly an order of magnitude as the operating regime is increased beyond telecom wavelengths.

| | | | |
|-----------------------------|------|-----|-----|
| λ (μm) | 1.55 | 1.8 | > 2 |
| FOM | 0.4 | 1 | > 3 |

Table 1.1: Nonlinear FOM over NIR and MIR wavelengths.

This combination of negligible 2PA and a strong n_2 near 2 μm has been exploited to demonstrate significantly improved efficiencies for silicon-based nonlinear processes, including FWM gain [79, 80], broadband SCG [81, 82], Raman amplification [83], and optical parametric oscillation [84]. Moving to longer wavelengths can improve the efficiency of nonlinear processes even further. Although the material nonlinearity n_2 is slightly lower beyond 2.4 μm than at telecom wavelengths (Fig. 1.5), there exists a key advantage due to the lack of significant 2PA. Multiphoton absorption is still present in the form of three-photon (3PA) and four-photon absorption (4PA), but the effect is much less severe [85, 86].

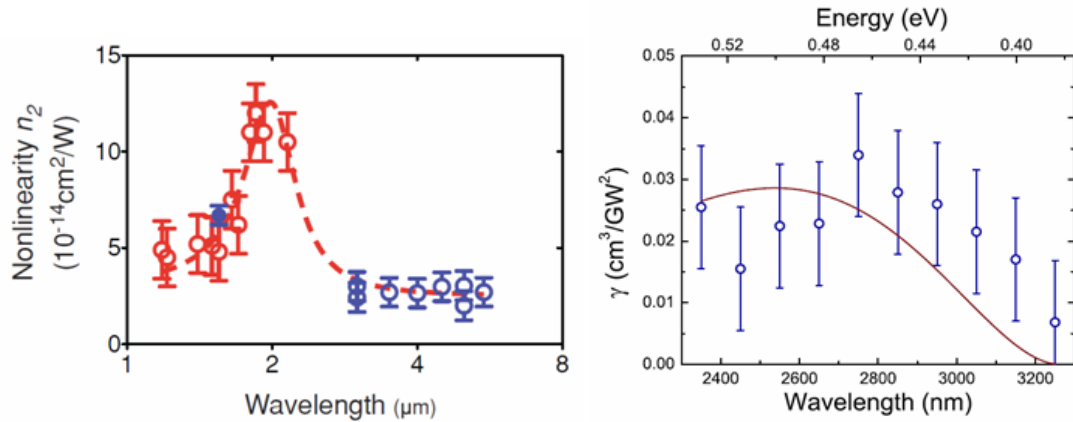


Figure 1.5: (a) Measurements of nonlinear index n_2 taken from Bristow et al. [31] and Gai et al. [86]. (b) Measurements of 3PA coefficient β_{3PA} taken from Pearl et al. [85].

The opportunities for silicon photonics in the MIR regime are abundant, and include applications in astronomy, chemical and biological spectroscopy, and free-space communications. For example, photonic technology has led to a reduction in size, weight, and complexity of astronomical instrumentation, and has the potential for an even larger impact at MIR wavelengths where interesting celestial objects can be

observed [87]. In addition, a large variety of chemical and biological substances exhibit strong fundamental vibrational absorption bands in the 2.5 – 25 μm range [88], where integrated photonics can provide a compact, chip-based sensing and detection solution. Even conventional high-speed telecom networks can benefit from development in the MIR, since an atmospheric transmission window exists at 3 – 5 μm [89]. Furthermore, the dominant loss mechanisms for these links arise from light scattering and scintillation which become mitigated with increasing wavelengths [90], making this regime an attractive prospect for free-space optical propagation links.

1.4 Thesis layout

In this thesis, we present recent work on nonlinear optical phenomena in silicon nanowaveguides for the MIR wavelength region. In Chapter 2, we introduce the numerical and experimental techniques used throughout this thesis. In Chapter 3, we present a numerical analysis of FWM in the 2- μm region, including nonlinear loss effects. In addition, we report the design and fabrication of silicon nanowaveguides and the demonstration of broadband, CW wavelength conversion between the telecom and MIR wavelength ranges. In Chapter 4, we report silicon-based, octave-spanning SCG characterized by soliton fission and dispersive wave generation. We also present a numerical analysis of the effects of 3PA and free-carrier effects on SCG and discuss the results from both low- and high-repetition-rate sources. In Chapter 5, we present an investigation of silicon microresonator-based frequency combs using a Lugiato-Lefever (LL) model modified to include multiphoton absorption and free-carrier effects, and discuss the implications of operating in the telecom and MIR wavelength ranges. In addition, we identify regimes in the MIR in which silicon microresonator-based broadband parametric oscillation may be achieved. In Chapter 6, we introduce a

novel waveguiding platform which uses standard SOI wafers, but has a top cladding of silicon nitride, transparent up to $6.6\ \mu\text{m}$. We also report the design, fabrication, and characterization of these nanowaveguides and the demonstration of broadband FWM near $2\ \mu\text{m}$. In Chapter 7, we present a summary of this work and a discussion on potential future directions for silicon-based nonlinear optics in the mid-infrared regime.

REFERENCES

- [1] T. H. Maiman, *Nature* **187**, 493 (1960).
- [2] K. C. Kao and G. A. Hockham, *Proceedings of the Institution of Electrical Engineers-London* **113**, 1151 (1966).
- [3] F. P. Kapron, D. B. Keck, and R. D. Maurer, *Appl. Phys. Lett.* **17**, 423 (1970).
- [4] S. E. Miller, *Bell System Technical Journal* **48**, 2059 (1969).
- [5] O. Wada, T. Sakurai, and T. Nakagami, *IEEE J. Quant. Electron.* **22**, 805 (1986).
- [6] T. L. Koch and U. Koren, *IEEE J. Quant. Electron.* **27**, 641 (1991).
- [7] O. Boyraz and B. Jalali, *Opt. Express* **12**, 5269 (2004).
- [8] M. A. Foster, A. C. Turner, J. E. Sharping, B. S. Schmidt, M. Lipson, and A. L. Gaeta, *Nature* **441**, 960 (2006).
- [9] B. Jalali, S. Yegnanarayanan, T. Yoon, T. Yoshimoto, I. Rendina, and F. Coppinger, *IEEE J. Sel. Topics Quant. Electron.* **4**, 938 (1998).
- [10] G. T. Reed and A. P. Knights, *Silicon Photonics: An Introduction* (Wiley, 2008).
- [11] G. T. Reed, G. Mashanovich, F. Y. Gardes, and D. J. Thomson, *Nature Photon.* **4**, 518 (2010).
- [12] D. Liang and J. E. Bowers, *Nature Photon.* **4**, 511 (2010).
- [13] J. Michel, J. F. Liu, and L. C. Kimerling, *Nature Photon.* **4**, 527 (2010).
- [14] M. A. Foster, K. D. Moll, and A. L. Gaeta, *Opt. Express* **12**, 2880 (2004).
- [15] A. C. Turner, C. Manolatou, B. S. Schmidt, M. Lipson, M. A. Foster, J. E. Sharping, and A. L. Gaeta, *Opt. Express* **14**, 4357 (2006).
- [16] L. H. Yin, Q. Lin, and G. P. Agrawal, *Opt. Lett.* **31**, 1295 (2006).
- [17] C. D. Salzberg and J. J. Villa, *J. Opt. Soc. Am.* **47**, 244 (1957).
- [18] Q. Lin, J. D. Zhang, P. M. Fauchet, and G. P. Agrawal, *Opt. Express* **14**, 4786 (2006).
- + [19] G. Agrawal, *Nonlinear Fiber Optics* (Academic Press, 2006).

- [20] R. W. Boyd, *Nonlinear Optics* (Academic Press, 2008).
- [21] J. K. Ranka, R. S. Windeler, and A. J. Stentz, *Opt. Lett.* **25**, 25 (2000).
- [22] J. M. Dudley, G. Genty, and S. Coen, *Rev. Mod. Phys.* **78**, 1135 (2006).
- [23] T. J. Kippenberg, S. M. Spillane, and K. J. Vahala, *Phys. Rev. Lett.* **93**, 4 (2004).
- [24] Q. Lin, T. J. Johnson, R. Perahia, C. P. Michael, and O. J. Painter, *Opt. Express* **16**, 10596 (2008).
- [25] S. Coen and M. Erkintalo, *Opt. Lett.* **38**, 1790 (2013).
- [26] M. R. E. Lamont, Y. Okawachi, and A. L. Gaeta, *Opt. Lett.* **38**, 3478 (2013).
- [27] J. F. Reintjes and J. C. McGroddy, *Phys. Rev. Lett.* **30**, 901 (1973).
- [28] H. K. Tsang, C. S. Wong, T. K. Liang, I. E. Day, S. W. Roberts, A. Harpin, J. Drake, and M. Asghari, *Appl. Phys. Lett.* **80**, 416 (2002).
- [29] M. Dinu, F. Quochi, and H. Garcia, *Appl. Phys. Lett.* **82**, 2954 (2003).
- [30] T. G. Euser and W. L. Vos, *J. Appl. Phys.* **97**, 7 (2005).
- [31] A. D. Bristow, N. Rotenberg, and H. M. van Driel, *Appl. Phys. Lett.* **90**, 3 (2007).
- [32] H. Garcia and R. Kalyanaraman, *J. Phys. B Atomic Molecular Opt. Phys.* **39**, 2737 (2006).
- [33] Q. Lin, O. J. Painter, and G. P. Agrawal, *Opt. Express* **15**, 16604 (2007).
- [34] M. A. Foster, A. C. Turner, M. Lipson, and A. L. Gaeta, *Opt. Express* **16**, 1300 (2008).
- [35] J. Leuthold, C. Koos, and W. Freude, *Nature Photon.* **4**, 535 (2010).
- [36] O. Boyraz, T. Indukuri, and B. Jalali, *Opt. Express* **12**, 829 (2004).
- [37] E. Dulkeith, Y. A. Vlasov, X. G. Chen, N. C. Panoiu, and R. M. Osgood, *Opt. Express* **14**, 5524 (2006).
- [38] I. W. Hsieh, X. G. Chen, J. I. Dadap, N. C. Panoiu, R. M. Osgood, S. J. McNab, and Y. A. Vlasov, *Opt. Express* **14**, 12380 (2006).
- [39] R. Dekker, A. Driessen, T. Wahlbrink, C. Moormann, J. Niehusmann, and M. Forst, *Opt. Express* **14**, 8336 (2006).

- [40] I. W. Hsieh, X. G. Chen, J. I. Dadap, N. C. Panoiu, R. M. Osgood, S. J. McNab, and Y. A. Vlasov, *Opt. Express* **15**, 1135 (2007).
- [41] W. Astar, J. B. Driscoll, X. P. Liu, J. I. Dadap, W. M. J. Green, Y. A. Vlasov, G. M. Carter, and R. M. Osgood, *Opt. Express* **17**, 12987 (2009).
- [42] R. L. Espinola, J. I. Dadap, R. M. Osgood, S. J. McNab, and Y. A. Vlasov, *Opt. Express* **13**, 4341 (2005).
- [43] K. Yamada, H. Fukuda, T. Tsuchizawa, T. Watanabe, T. Shoji, and S. Itabashi, *IEEE Photon. Technol. Lett.* **18**, 1046 (2006).
- [44] Y. H. Kuo, H. S. Rong, V. Sih, S. B. Xu, M. Paniccia, and O. Cohen, *Opt. Express* **14**, 11721 (2006).
- [45] H. S. Rong, Y. H. Kuo, A. S. Liu, M. Paniccia, and O. Cohen, *Opt. Express* **14**, 1182 (2006).
- [46] R. Salem, M. A. Foster, A. C. Turner, D. F. Geraghty, M. Lipson, and A. L. Gaeta, *Nature Photon.* **2**, 35 (2008).
- [47] Y. Okawachi, M. A. Foster, X. P. Chen, A. C. Turner-Foster, R. Salem, M. Lipson, C. Xu, and A. L. Gaeta, *Opt. Express* **16**, 10349 (2008).
- [48] Y. T. Dai, X. P. Chen, Y. Okawachi, A. C. Turner-Foster, M. A. Foster, M. Lipson, A. L. Gaeta, and C. Xu, *Opt. Express* **17**, 7004 (2009).
- [49] A. C. Turner-Foster, M. A. Foster, R. Salem, A. L. Gaeta, and M. Lipson, *Opt. Express* **18**, 1904 (2010).
- [50] I. W. Hsieh, X. G. Chen, X. P. Liu, J. I. Dadap, N. C. Panoiu, C. Y. Chou, F. N. Xia, W. M. Green, Y. A. Vlasov, and R. M. Osgood, *Opt. Express* **15**, 15242 (2007).
- [51] R. Claps, D. Dimitropoulos, V. Raghunathan, Y. Han, and B. Jalali, *Opt. Express* **11**, 1731 (2003).
- [52] R. L. Espinola, J. I. Dadap, R. M. Osgood, S. J. McNab, and Y. A. Vlasov, *Opt. Express* **12**, 3713 (2004).
- [53] H. S. Rong, A. S. Liu, R. Jones, O. Cohen, D. Hak, R. Nicolaescu, A. Fang, and M. Paniccia, *Nature* **433**, 292 (2005).
- [54] H. S. Rong, R. Jones, A. S. Liu, O. Cohen, D. Hak, A. Fang, and M. Paniccia, *Nature* **433**, 725 (2005).
- [55] B. Jalali, *Nature Photonics* **4**, 506 (2010).

- [56] V. R. Almeida, C. A. Barrios, R. R. Panepucci, and M. Lipson, *Nature* **431**, 1081 (2004).
- [57] D. J. Moss, L. Fu, I. Littler, and B. J. Eggleton, *Electron. Lett.* **41**, 320 (2005).
- [58] T. K. Liang, L. R. Nunes, T. Sakamoto, K. Sasagawa, T. Kawanishi, M. Tsuchiya, G. R. A. Priem, D. Van Thourhout, P. Dumon, R. Baets, and H. K. Tsang, *Opt. Express* **13**, 7298 (2005).
- [59] T. K. Liang, L. R. Nunes, M. Tsuchiya, K. S. Abedin, T. Miyazaki, D. Van Thourhout, W. Bogaerts, P. Dumon, R. Baets, and H. K. Tsang, *Opt. Comm.* **265**, 171 (2006).
- [60] R. Claps, V. Raghunathan, D. Dimitropoulos, and B. Jalali, *Opt. Express* **12**, 2774 (2004).
- [61] T. K. Liang and H. K. Tsang, *Appl. Phys. Lett.* **84**, 2745 (2004).
- [62] L. H. Yin and G. P. Agrawal, *Opt. Lett.* **32**, 2031 (2007).
- [63] Y. Liu and H. K. Tsang, *Applied Physics Letters* **90**, 3 (2007).
- [64] R. A. Soref, S. J. Emelett, and A. R. Buchwald, *J. Opt. A: Pure Appl. Opt.* **8**, 840 (2006).
- [65] R. Soref, *Nature Photon.* **4**, 495 (2010).
- [66] J. Faist, F. Capasso, D. L. Sivco, C. Sirtori, A. L. Hutchinson, and A. Y. Cho, *Science* **264**, 553 (1994).
- [67] Y. Yao, A. J. Hoffman, and C. F. Gmachl, *Nature Photon.* **6**, 432 (2012).
- [68] S. D. Jackson and T. A. King, *Opt. Lett.* **23**, 1462 (1998).
- [69] S. Tokita, M. Murakami, S. Shimizu, M. Hashida, and S. Sakabe, *Opt. Lett.* **34**, 3062 (2009).
- [70] S. D. Jackson, *Nature Photon.* **6**, 423 (2012).
- [71] T. J. Carrig, G. J. Wagner, A. Sennaroglu, J. Y. Jeong, and C. R. Pollock, *Opt. Lett.* **25**, 168 (2000).
- [72] I. T. Sorokina, *Mid-Infrared Coherent Sources and Applications*, 225 (2008).
- [73] J. H. Sun, B. J. S. Gale, and D. T. Reid, *Opt. Lett.* **32**, 1414 (2007).
- [74] F. Adler, K. C. Cossel, M. J. Thorpe, I. Hartl, M. E. Fermann, and J. Ye, *Opt. Lett.* **34**, 1330 (2009).

- [75] A. Schliesser, N. Picque, and T. W. Hansch, *Nature Photon.* **6**, 440 (2012).
- [76] T. Baehr-Jones, A. Spott, R. Ilic, B. Penkov, W. Asher, and M. Hochberg, *Opt. Express* **18**, 12127 (2010).
- [77] F. X. Li, S. D. Jackson, C. Grillet, E. Magi, D. Hudson, S. J. Madden, Y. Moghe, C. O'Brien, A. Read, S. G. Duvall, P. Atanackovic, B. J. Eggleton, and D. J. Moss, *Opt. Express* **19**, 15212 (2011).
- [78] Y. C. Chang, V. Paeder, L. Hvozدارa, J. M. Hartmann, and H. P. Herzig, *Opt. Lett.* **37**, 2883 (2012).
- [79] X. P. Liu, R. M. Osgood, Y. A. Vlasov, and W. M. J. Green, *Nature Photon.* **4**, 557 (2010).
- [80] B. Kuyken, X. P. Liu, G. Roelkens, R. Baets, R. M. Osgood, and W. M. J. Green, *Opt. Lett.* **36**, 4401 (2011).
- [81] B. Kuyken, X. P. Liu, R. M. Osgood, R. Baets, G. Roelkens, and W. M. J. Green, *Opt. Express* **19**, 20172 (2011).
- [82] U. D. Dave, S. Uvin, B. Kuyken, S. Selvaraja, F. Leo, and G. Roelkens, *Opt. Express* **21**, 32032 (2013).
- [83] V. Raghunathan, D. Borlaug, R. R. Rice, and B. Jalali, *Opt. Express* **15**, 14355 (2007).
- [84] A. G. Griffith, R. K. W. Lau, J. Cardenas, Y. Okawachi, A. Mohanty, R. Fain, Y. H. D. Lee, M. Yu, C. T. Phare, C. B. Poitras, A. L. Gaeta, and M. Lipson, *arXiv:1408.1039* (2014).
- [85] S. Pearl, N. Rotenberg, and H. M. van Driel, *Appl. Phys. Lett.* **93**, 3 (2008).
- [86] X. Gai, Y. Yu, B. Kuyken, P. Ma, S. J. Madden, J. Van Campenhout, P. Verheyen, G. Roelkens, R. Baets, and B. Luther-Davies, *Laser Photon. Rev.* **7**, 1054 (2013).
- [87] L. Labadie and O. Wallner, *Opt. Express* **17**, 1947 (2009).
- [88] F. K. Tittel, D. Richter, and A. Fried, *Solid-State Mid-Infrared Laser Sources* **89**, 445 (2003).
- [89] F. Capasso, R. Paiella, R. Martini, R. Colombelli, C. Gmachl, T. L. Myers, M. S. Taubman, R. M. Williams, C. G. Bethea, K. Unterrainer, H. Y. Hwang, D. L. Sivco, A. Y. Cho, A. M. Sergent, H. C. Liu, and E. A. Whittaker, *IEEE J. Quant. Electron.* **38**, 511 (2002).

- [90] P. F. Szajowski, G. Nykolak, J. J. Auburn, H. M. Presby, G. E. Tourgee, E. Korevaar, J. Schuster, and Kim, II, *Conference on Optical Wireless Communications* (Spie-Int Soc Optical Engineering, Boston, MA, 1998), pp. 29.

CHAPTER 2
NUMERICAL AND EXPERIMENTAL TECHNIQUES

2.1 Nonlinear Schrödinger equation

In the following chapters we investigate a variety of nonlinear optical processes, which can all be described by the nonlinear Schrödinger equation (NLSE). A commonly used form of the NLSE is given in the time domain as [1, 2]

$$\frac{\partial}{\partial z} A(z, \tau) = i \sum_{k \geq 2} \frac{\beta_k}{k!} \left(i \frac{\partial}{\partial \tau} \right)^k A(z, \tau) + i \gamma A(z, \tau) |A(z, \tau)|^2, \quad (2.1)$$

where $A(z, \tau)$ is the slowly varying field amplitude, β_k are the k^{th} -order terms in the Taylor expansion of the propagation constant $\beta(\omega) = \omega n(\omega)/c$, with $n(\omega)$ the refractive index of the propagating mode, $\gamma = n_2 \omega_0 / A_{\text{eff}} c$ is the nonlinear parameter, n_2 is the nonlinear index, and A_{eff} is the effective area of the propagating mode. This equation is expressed in the “retarded frame” through the transformation $\tau = t - z/v_g$, such that the frame of reference moves at the group velocity of the central frequency v_g .

Equation 2.1 is a simplified version of the NLSE, which, for certain cases, can be solved analytically to gain an intuition behind the various nonlinear processes. However, accurate modeling of experimental conditions typically requires additional terms to account for non-negligible processes such as linear and nonlinear losses, self-steepening, free-carrier effects, and Raman effects. Due to the interaction among the

nonlinear and linear processes, these terms introduce additional complexity to the NLSE, requiring computational methods for solution.

2.2 Split-step Fourier method

A common numerical approach to solving the NLSE is the split-step Fourier method (SSFM), which utilizes discrete steps in the time and frequency domain to separately address the nonlinear and linear terms, respectively [1]. Equation 2.1 can be rewritten as

$$\frac{\partial A}{\partial z} = i \sum_{k \geq 2} \frac{\beta_k}{k!} \left(i \frac{\partial}{\partial \tau} \right)^k A + i\gamma |A|^2 A = [\widehat{D} + \widehat{N}]A, \quad (2.2)$$

where \widehat{D} and \widehat{N} are the linear and nonlinear operators, respectively. The linear operator \widehat{D} is modeled in the frequency domain, and includes dispersion effects and linear absorption. The nonlinear operator \widehat{N} is modeled in the time domain, and describes any intensity-dependent effects, such as the Kerr effect, multiphoton absorption, and free-carrier effects.

An approximate solution of the NLSE can be obtained by propagating the pulse over a small step of size h and treating the operators \widehat{D} and \widehat{N} independently. After propagation, the field is then given by

$$A(z + h, \tau) = A(z, \tau) \exp(h\widehat{D}) \exp(h\widehat{N}). \quad (2.3)$$

2.3 Experimental techniques

In this section we describe several experimental techniques used throughout this thesis for free-space alignment of MIR beams and nanowaveguide¹ characterization. The procedure for input coupling of a MIR source to a nanowaveguide is done using a pair of pinhole irises, a thermal power meter, thermal cards sensitive to MIR and NIR wavelengths, a telecom source (amplified spontaneous emission from an amplifier will also suffice), a lensed tapered fiber, a chalcogenide aspheric lens, and at least two metallic mirrors (e.g., silver) for beam steering.

First the two pinhole irises are used to define the beam path of the MIR source. The first iris is placed immediately after the source, and the second is placed along the beam path a large distance away. By monitoring the transmitted power after each iris, fine adjustments are made to ensure that both irises are centered on the beam path. The irises and MIR source now remain fixed for the duration of the measurement, and all other beams will be adjusted such that they are collinear with the MIR source.

Next the telecom source is propagated backwards through the setup and made collinear with the MIR source. The lensed tapered fiber is mounted on a high-precision, three-axis translational stage and is used to couple the telecom source to the output facet of the nanowaveguide. Proper coupling to the nanowaveguide mode is ensured either by monitoring the transmitted mode profile on an infrared card or by monitoring the nanowaveguide from the top using an infrared camera. The telecom source is coupled out from the nanowaveguide using the aspheric lens mounted on a

¹ Nanowaveguides were fabricated by Professor Michal Lipson's group at the Cornell NanoScale Facility at Cornell University.

second identical translational stage. Two metallic mirrors are used to steer the telecom beam through the pinhole irises, such that both the telecom and MIR sources are now collinear. Finally, the telecom source at the nanowaveguide output is replaced with an optical spectrum analyzer or Fourier-transform infrared spectrometer for analysis of the MIR signal transmitted through the nanowaveguide.

For some experiments, such as the FWM measurement presented in Chapter 3, two MIR sources copropagate within the nanowaveguide. In such a case, first a beam splitter is placed near the output of the first MIR source. Then the first iris is placed after the beam splitter, and the MIR source is coupled into the nanowaveguide using the procedure outlined above. After the first MIR source has been properly aligned, the second MIR source is aligned through both irises using an additional mirror.

REFERENCES

- [1] G. Agrawal, *Nonlinear Fiber Optics* (Academic Press, 2006).
- [2] R. W. Boyd, *Nonlinear Optics* (Academic Press, 2008).

CHAPTER 3
**CONTINUOUS-WAVE FOUR-WAVE MIXING
IN THE MID-INFRARED REGION**

FWM is an optical phenomenon by which two frequencies in a nonlinear medium interact to produce two additional frequencies, and is governed by the third-order nonlinear susceptibility $\chi^{(3)}$ of the material [1, 2]. Using FWM-based silicon devices, many useful all-optical signal processing functionalities have been demonstrated in the telecom band, including parametric amplification [3], wavelength conversion [4-8], signal regeneration [9], and parametric delay [10, 11]. While their efficiencies in this wavelength range are fundamentally limited by 2PA and FCA, relatively large amplification has been demonstrated in silicon photonic devices operating near 2.2 μm [12, 13].

Other reports of MIR FWM in silicon nanowaveguides have used a pulsed pump source [12-15], but a number of applications, such as free-space communications, would require the use of a continuous-wave (CW) pump. A CW pump would facilitate wavelength conversion of a continuous data stream and allow transfer of amplitude and phase modulation between the signal and idler, enabling the creation and detection of modulated signals at MIR wavelengths where modulators and high-speed detectors are not readily available. In this chapter², we present a numerical analysis of FWM in silicon nanowaveguides in the 2- μm region. We design and fabricate devices, and demonstrate broadband, CW wavelength conversion between the telecom and MIR wavelength ranges.

² R. K. W. Lau, M. Ménard, Y. Okawachi, M. A. Foster, A. C. Turner-Foster, R. Salem, M. Lipson, and A. L. Gaeta, *Opt. Lett.* **36**, 1263 (2011).

3.1 Energy conservation and phase matching

In this work, we consider degenerate FWM, in which two photons from a pump field at frequency ω_p are converted to signal and idler photons at frequencies ω_s and ω_i , respectively, such that $2\omega_p = \omega_s + \omega_i$ (Fig. 3.1). The generation of these additional photons can therefore result in amplification of the original signal field as well as frequency conversion from the signal wavelength to the idler wavelength.

Efficient FWM over broad bandwidths requires minimizing the phase mismatch due to the interacting pump, signal, and idler fields and the nonlinear effects introduced by the pump [3, 16, 17]. The propagating fields have a linear contribution to the phase mismatch given by $\Delta k_L = 2k_p - k_s - k_i$, and the pump has a nonlinear contribution given by $\Delta k_{NL} = 2\gamma P_p$. Consequently, in order to minimize the total phase mismatch $\Delta k = \Delta k_{NL} - \Delta k_L = 2\gamma P_p - (2k_p - k_s - k_i)$, the total linear contribution must be positive. Equivalently, the wavenumber of the pump must be slightly greater than the average of the signal and idler wavenumbers (Fig. 3.1). This condition corresponds to slightly anomalous GVD at the pump wavelength (i.e., pumping on the anomalous side of the zero-GVD wavelength), resulting in the linear phase mismatch compensating the pump-induced nonlinear phase shift. The ability to engineer the GVD of nanowaveguides, in addition to the large material nonlinearity of silicon, has enabled broadband parametric gain and wavelength conversion via FWM in CMOS-compatible devices.

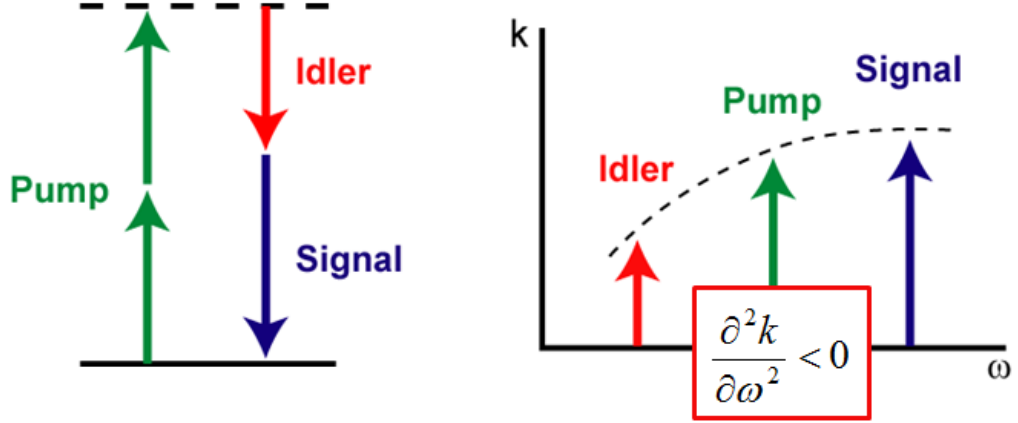


Figure 3.1: FWM energy and momentum diagrams. The phase matching condition requires the wavenumber of the pump to be slightly greater than the average of the signal and idler wavenumbers. This corresponds to a regime of anomalous GVD.

3.2 Numerical modeling of four-wave mixing process

We model the FWM process in the silicon nanowaveguides using the following coupled differential equations for the pump A_p , signal A_s , and idler A_i fields [1, 16]:

$$\frac{dA_p}{dz} = -\frac{1}{2}[\alpha_{in}^p + \beta_{TPA}I_p + \alpha_{FCA}^p I_p^2]A_p + i\gamma|A_p|^2 A_p, \quad (3.1)$$

$$\begin{aligned} \frac{dA_s}{dz} = & -\frac{1}{2}[\alpha_{in}^s + 2\beta_{TPA}I_p + \alpha_{FCA}^s I_p^2]A_s + 2i\gamma|A_p|^2 A_s \\ & + i\gamma A_p^2 A_i^* e^{(i\Delta kz)}, \end{aligned} \quad (3.2)$$

$$\begin{aligned} \frac{dA_i}{dz} = & -\frac{1}{2}[\alpha_{in}^i + 2\beta_{TPA}I_p + \alpha_{FCA}^i I_p^2]A_i + 2i\gamma|A_p|^2 A_i \\ & + i\gamma A_p^2 A_s^* e^{(i\Delta kz)}, \end{aligned} \quad (3.3)$$

where $I_p = |A_p|^2/A_{eff}$ is the pump intensity; A_{eff} is the effective area of the nanowaveguide mode; α_{lin}^p , α_{lin}^s , and α_{lin}^i are the linear propagation loss coefficients at the pump, signal, and idler wavelengths, respectively; β_{TPA} is the 2PA coefficient at the pump wavelength; $\Delta k = 2k_p - k_s - k_i$ is the linear phase mismatch; k_p , k_s , and k_i are the wavenumbers of the pump, signal, and idler, respectively; $\gamma = 2\pi n_2/\lambda_p A_{eff}$ is the effective nonlinearity of the nanowaveguide; n_2 is the nonlinear index coefficient; and λ_p is the pump wavelength. The FCA coefficient due to 2PA is given by [18]

$$\alpha_{FCA}(\lambda) = 1.45 \times 10^{-21} [\text{m}^2] \left(\frac{\lambda_p}{1.55 \times 10^{-6} [\text{m}]} \right)^2 \left(\frac{\beta_{TPA} \tau_{eff} \lambda}{2hc} \right), \quad (3.4)$$

where τ_{eff} is the effective free-carrier lifetime, h is Planck's constant, c is the speed of light in vacuum, and all numeric quantities are given in meters.

3.3 Nanowaveguide design and fabrication

The GVD for the fundamental transverse electric (TE) mode of the nanowaveguides is modeled using a custom finite-difference mode solver and is shown for varying cross sections in Fig. 3.2. The effective index values resulting from the mode solver are then used in numerical integration of Eqs. (3.1 – 3.3) to determine the optimal nanowaveguide dimensions for maximum FWM conversion bandwidth with a 2- μm pump source. We find that a cross section of 950 nm by 280 nm results in a zero-GVD wavelength of 1950 nm (inset, Fig. 3.2.), which is within the tuning range of our source.

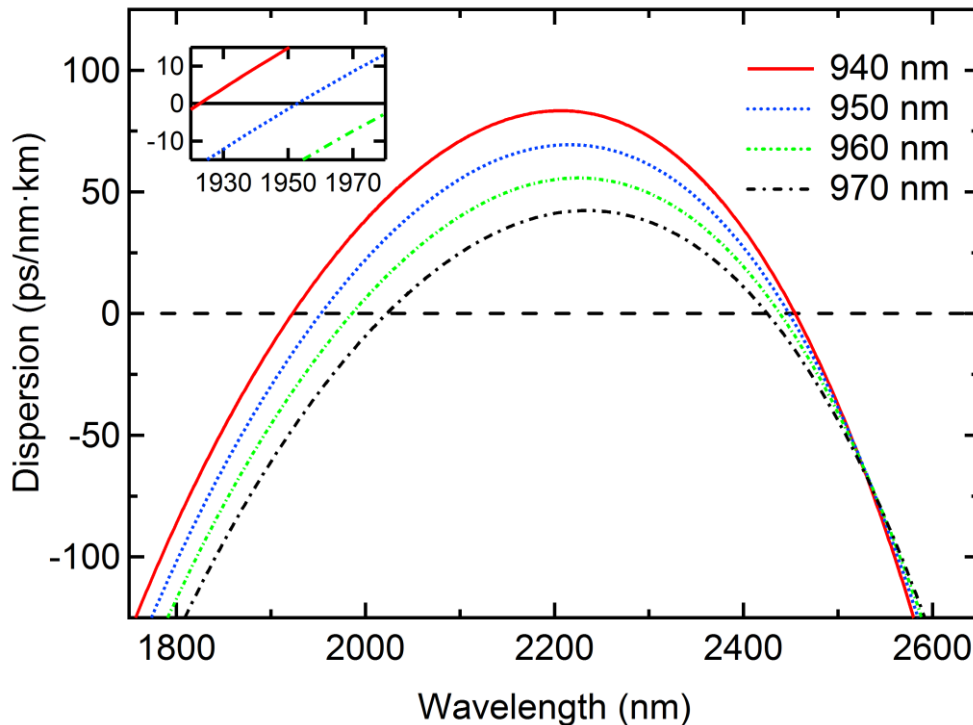


Figure 3.2: Simulated GVD for the TE mode of nanowaveguides with widths ranging from 940 nm to 970 nm and a height of 280 nm.

The silicon nanowaveguides are fabricated³ on an SOI wafer with a 3- μm buried oxide and a 500-nm silicon layer. The silicon slab is thinned by wet oxidation, and the nanowaveguides are patterned with electron-beam lithography before being dry etched with SF_6 chemistry and clad with 3 μm of SiO_2 by PECVD. Inverted tapers narrowing to 250 nm are added to the input and output facets to facilitate coupling between the free-space and fundamental TE waveguide modes [19]. Each nanowaveguides is 1 cm long and designed in a spiral layout with a footprint of 1 mm^2 . A silicon chip containing five such nanowaveguides is shown in Fig. 3.3.

³ Fabrication done by Dr. Michaël Ménard in Professor Michal Lipson's group at Cornell University.

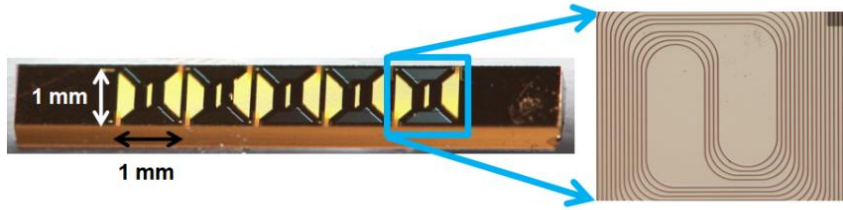


Figure 3.3: Image of silicon chip containing five nanowaveguides, each having a 1 mm² footprint.

3.4 Experimental demonstration of wavelength conversion

The pump source used in the experiment is a high-power CW thulium fiber laser with a tuning range of 1940 nm to 1970 nm (IPG Photonics). Two different signal sources are used, the first a CW thulium fiber laser tunable from 1790 nm to 1970 nm (PicoLuz), and the second a CW Cr²⁺:ZnSe bulk laser tunable from 2200 nm to 2422 nm (IPG Photonics). The TE polarization mode is selected for the pump and signal beams using a polarization beam-splitter cube and polarization controller, respectively. The pump and signal beams are combined with a pellicle beam splitter and coupled into the silicon nanowaveguide using an aspheric lens. The output of the nanowaveguide is coupled through a tapered fiber and sent to an optical spectrum analyzer (OSA) (Yokogawa). The experimental setup is shown in Fig. 3.4.

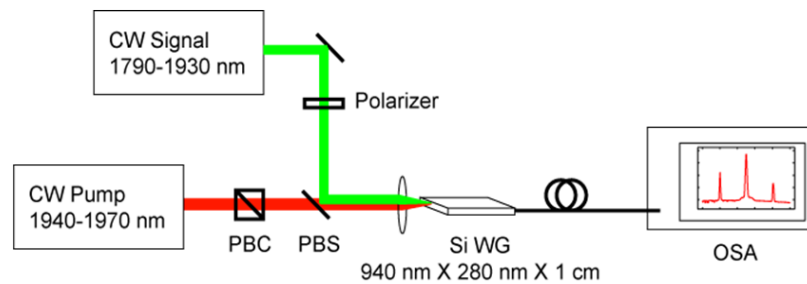


Fig. 3.4: Experimental setup of FWM-based wavelength conversion. PBC, polarization beam cube; PBS pellicle beam splitter; Si WG, silicon nanowaveguide; OSA, optical spectrum analyzer.

We first characterize the nanowaveguide loss using the cut-back method on a chip containing nanowaveguide with varying lengths [20]. At 1950 nm, the propagation loss and input/output coupling loss are estimated to be -1.7 dB/cm and -3 dB/facet, respectively.

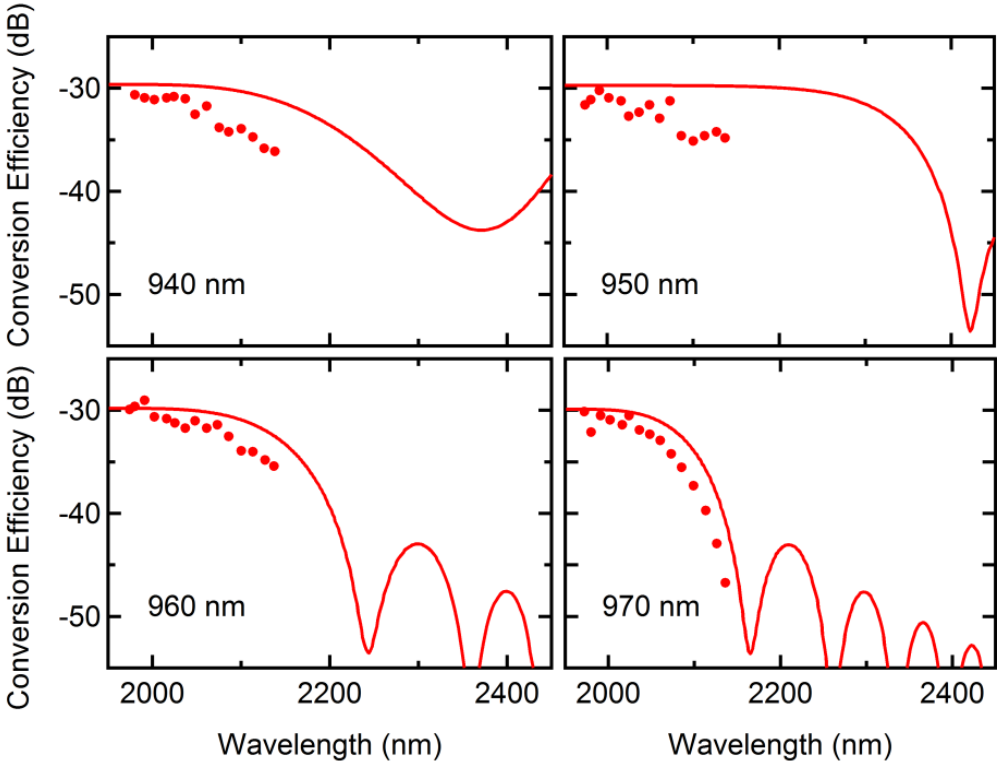


Fig. 3.5: Theoretical (lines) and measured (dots) conversion efficiencies as functions of idler wavelengths for nanowaveguides of varying widths.

We investigate the dependence of parametric bandwidth on GVD by measuring the FWM wavelength conversion efficiency, defined here as the ratio of output idler power to output signal power. The nanowaveguide widths range from 940 nm to 970 nm, the heights are all 280 nm, and the lengths are all 1 cm. For each nanowaveguide, the pump wavelength is fixed at 1950 nm, and the conversion efficiency is measured as the signal wavelength is continuously tuned from 1790 nm

to 1930 nm. The pump and signal powers inside the nanowaveguide are estimated to be 30 mW and 300 μ W, respectively. The experimental results are plotted in Fig. 3.5 along with the expected theoretical conversion efficiencies calculated in Section 3.2.

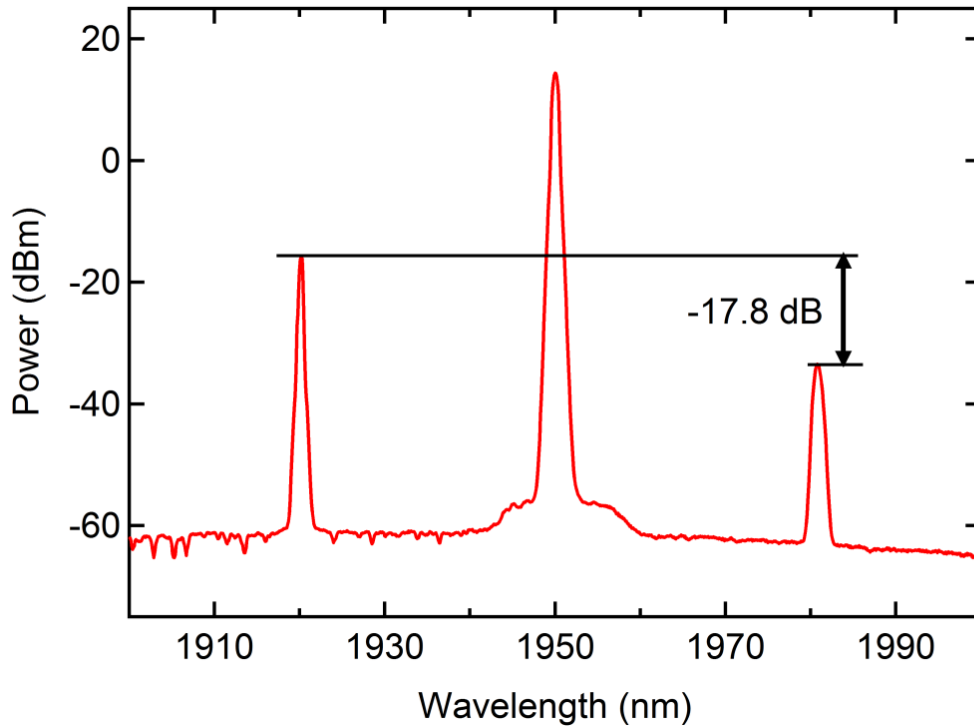


Fig. 3.6: FWM showing -17.8 dB of conversion efficiency with 160 mW of CW pump power at 1950 nm.

We find that the theoretical conversion bandwidth using a 1950-nm pump is broadest for the nanowaveguide width of 950 nm, consistent with the dispersion profiles presented in Section 3.3. Furthermore, we observe excellent qualitative agreement between the measured and expected conversion bandwidths for the varying nanowaveguides, particularly the rapid decrease of the conversion efficiency beyond 2.1 μ m for the 970-nm-wide nanowaveguide. At these power levels, the measured peak conversion efficiency occurring at small signal-idler detunings is approximately

-30 dB, which is in good agreement with theoretical predictions. For an increased pump power of 160 mW, the maximum conversion efficiency is measured to be -17.8 dB (Fig. 3.6). Further increase of pump power has resulted in damage of the nanowaveguides input tapers. Pump saturation due to nonlinear losses has not been observed at these power levels.

We next demonstrate broadband wavelength conversion using a 940-nm-wide nanowaveguide and 1940-nm pump, corresponding to the maximum theoretical 3-dB conversion bandwidth within our experimental constraints. Figure 3.7(a) shows the measured FWM spectra as the signal (thulium fiber laser) is tuned from 1792 nm to 1928 nm. Figure 3.7(b) shows the corresponding measured and theoretical conversion efficiencies as functions of idler wavelength. Wavelength conversion occurs from the short-wavelength side of the pump to the long-wavelength side. With 25 mW of pump power, the conversion efficiency ranges from -31.7 dB to -34 dB, varying less than 3 dB across the entire tuning range of the signal.

In order to demonstrate wavelength conversion over a broader bandwidth, the thulium fiber laser is replaced by the $\text{Cr}^{2+}:\text{ZnSe}$ bulk laser as the signal source. Figures 3.7(c) and (d) show the measured FWM spectra and corresponding conversion efficiency, respectively, as the signal ($\text{Cr}^{2+}:\text{ZnSe}$ bulk laser) is tuned from 2172 nm to 2422 nm. Here wavelength conversion occurs from the long-wavelength side of the pump to the short-wavelength side.

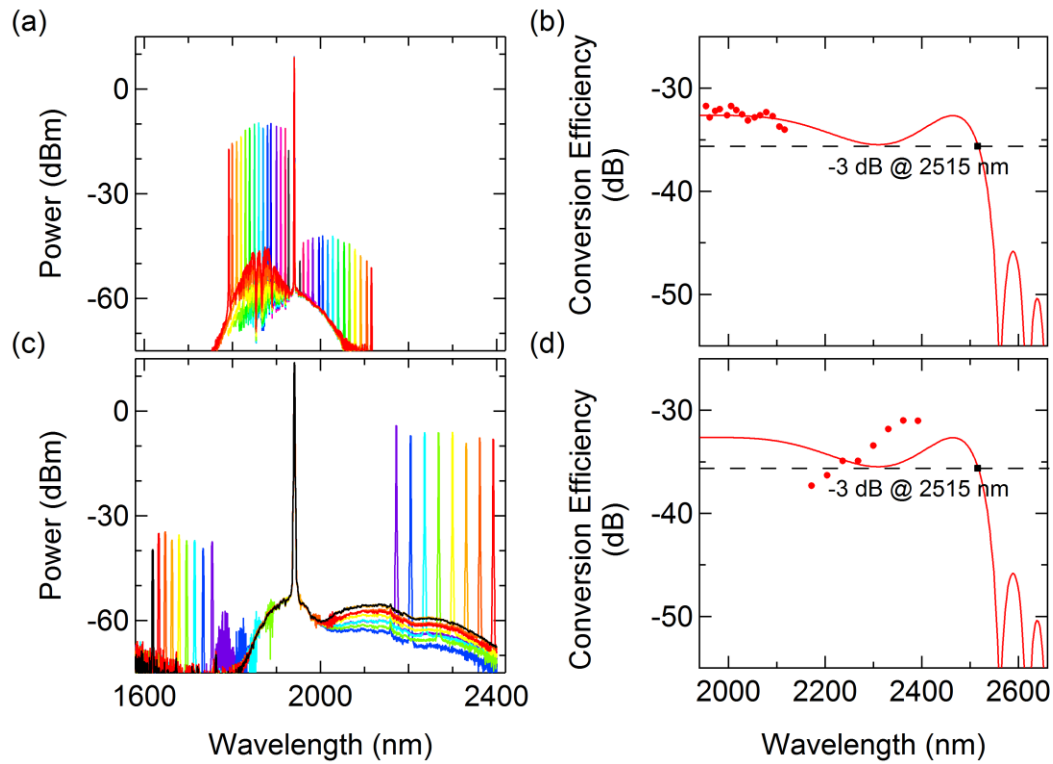


Fig. 3.7: (a) Measured FWM spectra as signal is tuned from (a) 1792 nm to 1928 nm and (c) 2172 nm to 2422 nm. Corresponding theoretical (lines) and measured (dots) conversion efficiencies are shown in (b) and (d). Theoretical 3-dB conversion bandwidth extends to 2515 nm.

We note that the longest signal wavelength of 2422 nm lies beyond the OSA detection limit of 2.4 μm . However, we observe the wavelength-converted idler as expected from energy conservation of the FWM process between the 1940-nm pump and 2422-nm signal, shown in black at 1619 nm in Fig. 3.7. The wavelength conversion from 2422 nm to 1619 nm corresponds to 803 nm of FWM bandwidth, and is limited only by the wavelength range of the signal lasers. The full 3-dB conversion bandwidth is shown theoretically to be 936 nm, spanning from 1579 nm to 2515 nm. The conversion efficiency across the tuning range of signal ranges from -27 dB to -33 dB. Measured conversion efficiencies for the longer wavelengths are higher than expected, and may be attributed to inefficient collection of the signal power at the

nanowaveguide output. The output is collected with a silica tapered fiber designed for telecom wavelengths, and since the conversion efficiency is defined here as the ratio of idler to signal power at the nanowaveguide output, a reduction in detected signal power would give the appearance of increased conversion efficiency.

3.5 Summary

In this chapter we have reported the first demonstration of CW FWM in silicon nanowaveguides for the MIR region. We have designed and fabricated devices with a zero-GVD wavelength near 2 μm , enabling broadband wavelength conversion between telecom and MIR wavelengths. We have achieved experimentally a continuous FWM bandwidth across 803 nm, from 1619 nm to 2422 nm, and have shown theoretically a bandwidth across 936 nm, from 1579 nm to 2515 nm. Demonstrating their utility in potential free-space communications systems, these devices have also been used for data generation and reception in the 2- μm region [21]. Taken together, these results illustrate the potential for silicon photonics in a large range of MIR applications which require CW operation.

REFERENCES

- [1] G. Agrawal, *Nonlinear Fiber Optics* (Academic Press, 2006).
- [2] R. W. Boyd, *Nonlinear Optics* (Academic Press, 2008).
- [3] M. A. Foster, A. C. Turner, J. E. Sharping, B. S. Schmidt, M. Lipson, and A. L. Gaeta, *Nature* **441**, 960 (2006).
- [4] R. L. Espinola, J. I. Dadap, R. M. Osgood, S. J. McNab, and Y. A. Vlasov, *Opt. Express* **13**, 4341 (2005).
- [5] K. Yamada, H. Fukuda, T. Tsuchizawa, T. Watanabe, T. Shoji, and S. Itabashi, *IEEE Photon. Technol. Lett.* **18**, 1046 (2006).
- [6] Y. H. Kuo, H. S. Rong, V. Sih, S. B. Xu, M. Paniccia, and O. Cohen, *Opt. Express* **14**, 11721 (2006).
- [7] H. S. Rong, Y. H. Kuo, A. S. Liu, M. Paniccia, and O. Cohen, *Opt. Express* **14**, 1182 (2006).
- [8] A. C. Turner-Foster, M. A. Foster, R. Salem, A. L. Gaeta, and M. Lipson, *Opt. Express* **18**, 1904 (2010).
- [9] R. Salem, M. A. Foster, A. C. Turner, D. F. Geraghty, M. Lipson, and A. L. Gaeta, *Nature Photon.* **2**, 35 (2008).
- [10] Y. Okawachi, M. A. Foster, X. P. Chen, A. C. Turner-Foster, R. Salem, M. Lipson, C. Xu, and A. L. Gaeta, *Opt. Express* **16**, 10349 (2008).
- [11] Y. T. Dai, X. P. Chen, Y. Okawachi, A. C. Turner-Foster, M. A. Foster, M. Lipson, A. L. Gaeta, and C. Xu, *Opt. Express* **17**, 7004 (2009).
- [12] X. P. Liu, R. M. Osgood, Y. A. Vlasov, and W. M. J. Green, *Nature Photon.* **4**, 557 (2010).
- [13] B. Kuyken, X. P. Liu, G. Roelkens, R. Baets, R. M. Osgood, and W. M. J. Green, *Opt. Lett.* **36**, 4401 (2011).
- [14] S. Zlatanovic, J. S. Park, S. Moro, J. M. C. Boggio, I. B. Divliansky, N. Alic, S. Mookherjea, and S. Radic, *Nature Photon.* **4**, 561 (2010).
- [15] X. P. Liu, B. Kuyken, G. Roelkens, R. Baets, R. M. Osgood, and W. M. J. Green, *Nature Photon.* **6**, 667 (2012).

- [16] Q. Lin, J. D. Zhang, P. M. Fauchet, and G. P. Agrawal, *Opt. Express* **14**, 4786 (2006).
- [17] M. R. E. Lamont, B. T. Kuhlmeier, and C. M. de Sterke, *Opt. Express* **16**, 7551 (2008).
- [18] R. Claps, V. Raghunathan, D. Dimitropoulos, and B. Jalali, *Opt. Express* **12**, 2774 (2004).
- [19] V. R. Almeida, R. R. Panepucci, and M. Lipson, *Opt. Lett.* **28**, 1302 (2003).
- [20] G. T. Reed and A. P. Knights, *Silicon Photonics: An Introduction* (Wiley, 2008).
- [21] N. Ophir, R. K. W. Lau, M. Menard, R. Salem, K. Padmaraju, Y. Okawachi, M. Lipson, A. L. Gaeta, and K. Bergman, *IEEE Photon. Technol. Lett.* **24**, 276 (2012).

CHAPTER 4

MID-INFRARED SUPERCONTINUUM GENERATION

SCG is characterized by the spectral broadening of high-power, ultrashort pulses via propagation through nonlinear media, and has found many applications in frequency metrology [1], optical coherence tomography [2], and microscopy [3]. Photonic waveguides can greatly facilitate broadband SCG, since the modal confinement enables an enhanced nonlinearity and the potential for GVD engineering. While significant work on broadband SCG has been pioneered in microstructured optical fibers [4-9], the drive for an integrated, chip-based solution has led to the emergence of several attractive platforms, including chalcogenide glass [10, 11], high-index glass [12], silicon nitride [13], and silicon [14-16].

As discussed in Chapter 1, silicon-based SCG suffers from the nonlinear loss mechanisms of 2PA and FCA at telecom wavelengths, though these effects can be mitigated by pumping beyond 2.2 μm . While SCG in the MIR wavelength range has been previously demonstrated in silicon nanowaveguides [15, 16], the generated spectra were limited to 1000 nm, since the broadening was dominated mainly by modulation instability. It is well known that larger bandwidths can be obtained by using femtosecond pump pulses in the anomalous GVD regime, resulting in spectral broadening dominated mainly by soliton-related dynamics [9]. It has been shown that the existence of zero-GVD wavelengths can result in the generation of dispersive waves on both the long- and short-wavelength sides of the pump, further broadening the generated supercontinuum [5, 6, 8]. In this chapter⁴, we present a fundamentally

⁴R. K. W. Lau, M. R. E. Lamont, A. G. Griffith, Y. Okawachi, M. Lipson, and A. L. Gaeta, *Opt. Lett.* **39**, 4518 (2014).

different SCG, characterized by soliton fission and dispersive wave generation across two zero-GVD wavelengths, and report the first silicon-based, octave-spanning SCG as well as the longest wavelength generated via SCG in a silicon nanowaveguide. In addition, we present a numerical analysis of the effects of 3PA and free-carrier effects on SCG and compare the results from both low- and high-repetition-rate sources.

4.1 Numerical modeling of supercontinuum generation dynamics

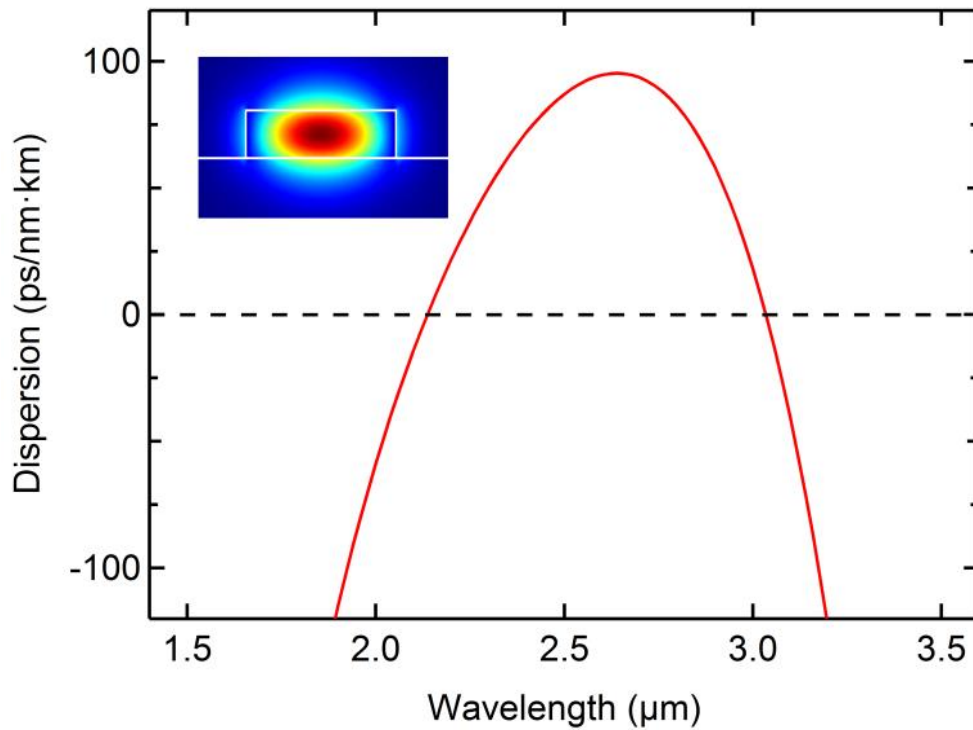


Figure 4.1: Simulated GVD for TE mode of nanowaveguide with cross section of 1210 nm by 320 nm, resulting in anomalous GVD near 2.5- μm pump and zero-GVD wavelengths near 2.1 μm and 3.0 μm . Mode profile shown in inset.

The silicon nanowaveguide is 1210 nm wide, 320 nm tall, and 2 cm long, and has been designed to facilitate broadband SCG through soliton fission and dispersive wave

generation using a 2.5- μm pump. The GVD for the fundamental TE mode is modeled using a custom finite-difference mode solver, as in the previous chapter, and is anomalous over the tuning range of the pump, with zero-GVD wavelengths near 2.1 μm and 3.0 μm (Fig. 4.1). The nanowaveguide cross section and mode profile at $\lambda = 2.5 \mu\text{m}$ are shown in the inset.

We investigate the SCG spectral and temporal dynamics in the silicon nanowaveguide by modeling the pulse evolution using the following nonlinear Schrödinger equation, which includes 3PA and free-carrier effects [17-19]:

$$\begin{aligned} \frac{\partial A}{\partial z} = & -\frac{\alpha}{2}A + \sum_{k \geq 2} i^{k+1} \frac{\beta_k}{k!} \frac{\partial^k A}{\partial \tau^k} \\ & + \left(1 + \frac{i}{\omega_0} \frac{\partial}{\partial \tau}\right) \left(i\gamma |A|^2 A - \frac{\gamma_{3PA}}{2A_{eff}^2} |A|^4 A \right) - \frac{\sigma}{2} (1 + i\mu) N_c A, \end{aligned} \quad (4.1)$$

where $A(z, \tau)$ is the envelope of the electric field, α is the linear loss, β_k are the dispersion coefficients at the central frequency ω_0 of the pulse, $\tau = t - \beta_1 z$ is the retarded time, $\gamma = 2\pi n_2 / \lambda_p A_{eff}$ is the effective nonlinearity of the nanowaveguide, n_2 is the nonlinear index coefficient, A_{eff} is the effective area of the nanowaveguide mode, λ_p is the pump wavelength, γ_{3PA} is the 3PA coefficient, σ and μ are the FCA cross section and FCD parameters, respectively [20, 21], and N_c is the free-carrier density. The carrier generation rate is determined by 3PA, and the recombination rate is captured by an effective free-carrier lifetime τ_{eff} , such that

$$\frac{\partial N_c}{\partial \tau} = \frac{\gamma_{3PA}}{3\hbar\omega_0} \frac{|A|^6}{A_{eff}^3} - \frac{N_c}{\tau_{eff}}. \quad (4.2)$$

We numerically solve Eqs. (4.1) and (4.2) using the split-step Fourier method [17], with values $n_2 = 9 \times 10^{-14} \text{ cm}^2/\text{W}$, $\gamma_{3PA} = 0.025 \text{ cm}^3/\text{GW}^2$, $\sigma = 3.7 \times 10^{-21} \text{ m}^2$, and $\mu = 4.7$, as taken from literature [21-23]. We use a value of $\tau_{eff} = 10 \text{ ns}$ for the free-carrier lifetime, taken as an upper estimate from the measurements of smaller but similar devices [24].

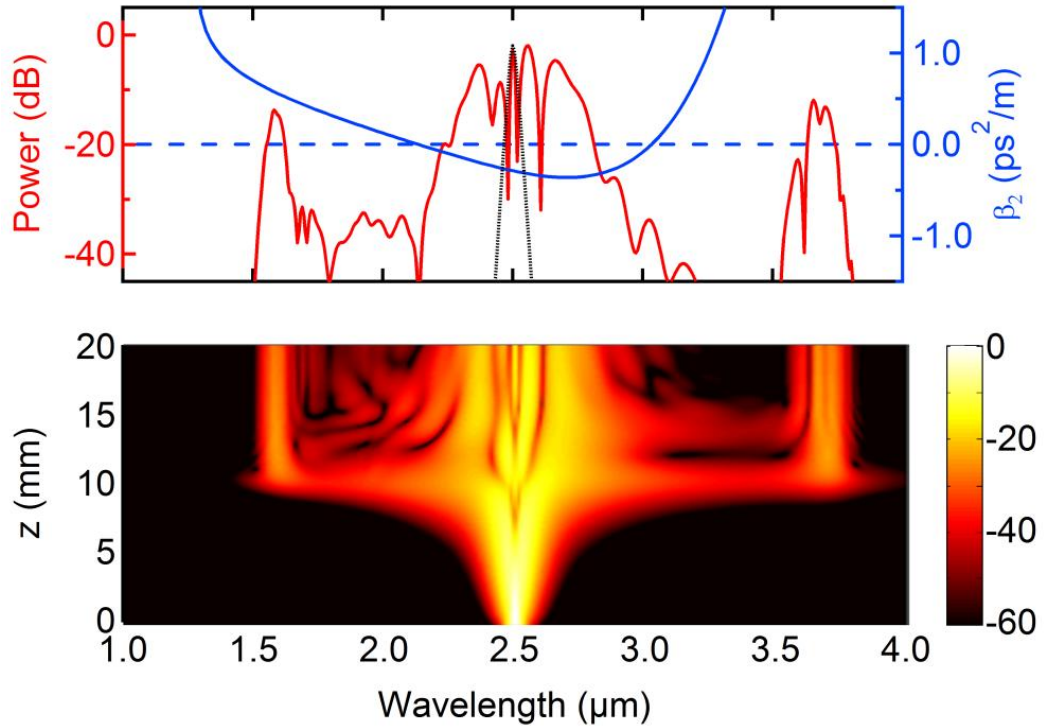


Fig. 4.2: Simulated SCG with $\lambda_p = 2.5 \mu\text{m}$, $T_0 = 300 \text{ fs}$, and $P_0 = 15 \text{ W}$. Output supercontinuum spectrum (red), input pulse spectrum (black), and waveguide dispersion (blue) are shown at top. Spectral evolution along silicon nanowaveguide shown at bottom.

The spectral evolution of a hyperbolic secant pulse along the silicon nanowaveguide is simulated and presented in Fig. 4.2. The pulse properties are modeled from the OPO system described in Section 4.2. The pump wavelength, pulse width, and peak power are $\lambda_p = 2.5 \mu\text{m}$, $T_0 = 300 \text{ fs}$, and $P_0 = 15 \text{ W}$, respectively.

We observe an initial stage of spectral broadening and temporal compression, followed by soliton fission halfway along the 2-cm-long nanowaveguide and the subsequent formation of short-wavelength and long-wavelength dispersive waves in the normal-GVD regime. The soliton number is a function of the characteristic dispersive and nonlinear length scales, given by $N = \sqrt{L_D/L_{NL}} = 10$ [9]. This corresponds to an expected soliton fission length of $L_{fiss} \sim L_D/N = 1$ cm, consistent with simulation results. For a soliton of peak power P_S and frequency ω_S , the frequency of the dispersive wave ω_{DW} satisfies the relation [9]

$$\beta(\omega_S) - \frac{\omega_S}{v_{g,s}} + (1 - f_R)\gamma P_S = \beta(\omega_{DW}) - \frac{\omega_{DW}}{v_{g,s}}, \quad (4.3)$$

where $v_{g,s}$ is the soliton group velocity at ω_S .

4.2 Experimental demonstration of supercontinuum generation

The silicon nanowaveguides are fabricated⁵ on an SOI wafer as described in Ref. [25]. They are pumped near 2.5 μm with 300 fs pulses from an OPO at a repetition rate of 80 MHz. The pulses have an average power of 3 mW and are coupled into and out of the nanowaveguide using aspheric chalcogenide lenses. The peak power of the OPO idler pulses is 125 W, and with an input coupling loss of 9 dB, we estimate an on-chip peak power of approximately 15 W. The output spectra are measured using an FTIR with a liquid nitrogen-cooled detector.

⁵ Fabrication done by Austin G. Griffith in Professor Michal Lipson's group at Cornell University.

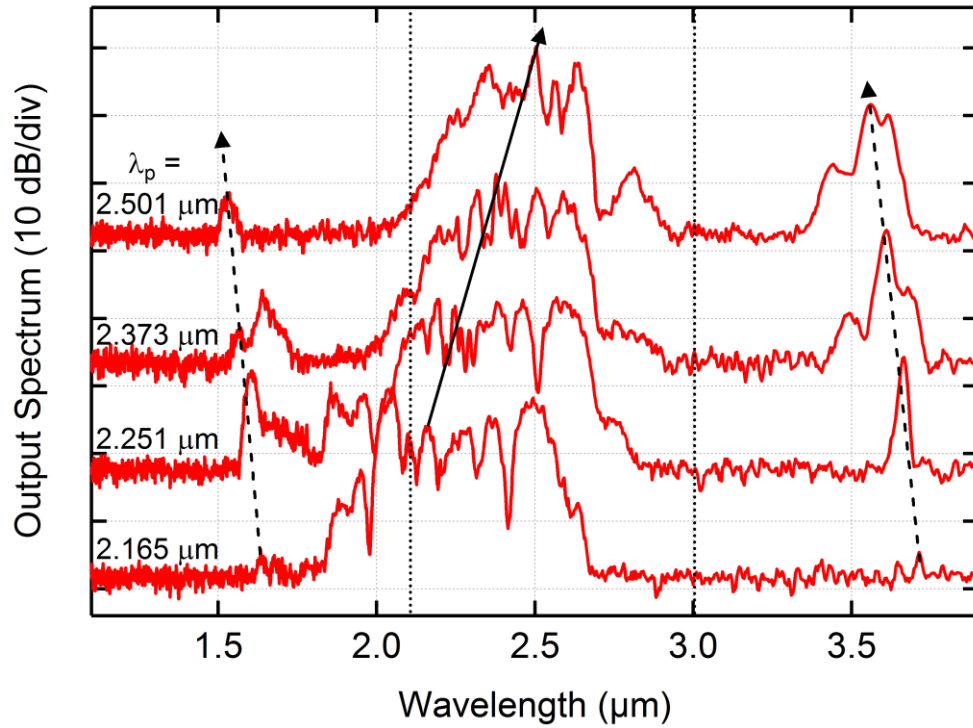


Fig 4.3: Experimentally measured output spectra as the pump is tuned from 2.165 nm to 2.501 nm, as indicated by the black solid line. From bottom to top, the spectra correspond to pump wavelengths of 2.165, 2.251, 2.373, and 2.501 μm . Dashed lines show the resulting shift of dispersive waves generated near 1.5 μm and 3.6 μm . Zero-GVD wavelengths at 2.1 μm and 3.0 μm are indicated by dotted lines.

Figure 4.3 shows the resulting SCG from the nanowaveguide output for varying pump wavelengths between 2.16 μm to 2.50 μm . We observe spectral broadening of more than 1000 nm near the pump, as well as the generation of dispersive waves near 1.5 μm and 3.6 μm . As the pump wavelength is tuned from the normal-GVD regime near 2.1 μm toward the anomalous-GVD regime near 2.5 μm , we observe the corresponding wavelength shift of both dispersive waves. The telecom dispersive wave blueshifts since the pump moves away from the zero-GVD wavelength at 2.1 μm , while the MIR dispersive wave redshifts since the pump moves closer to the zero-GVD wavelength at 3.0 μm , as expected from phase matching

conditions [9].

We note that the experimental results show a much weaker telecom dispersive wave compared to the MIR dispersive wave, whereas simulations predict both waves to have similar power levels. We attribute the relatively weak telecom dispersive wave to two effects. The first is the chromatic aberration of the collection optics and nanowaveguide tapers, which are optimized by MIR wavelengths, thus reducing the measured power received by the detector at 1.5 μm . The second is the presence of 2PA at telecom wavelengths, which has not been included in simulations. We also note that the dynamic range of the FTIR is limited to 25 dB, so the weaker spectral features predicted by simulations are below the noise floor and are not experimentally observable here.

4.3 Three-photon absorption and free-carrier effects from low- and high-repetition-rate sources

We numerically investigate the effects of 3PA and free carriers on SCG in the wavelength region beyond 2.2 μm . Figure 4.4(a) shows a comparison of the various effects on SCG, using the same parameters as the experiment described in Section 4.2 ($\lambda_p = 2.5 \mu\text{m}$, $T_0 = 300 \text{ fs}$, and $P_0 = 15 \text{ W}$). The dashed black line shows the spectrum generated in the absence of 3PA ($\gamma_{3PA} = 0$). The dotted blue line shows the spectrum generated in the presence of 3PA but not free-carriers ($\gamma_{3PA} \neq 0$, σ and $\mu = 0$). The solid red line shows the spectrum generated in the presence of all nonlinear effects (γ_{3PA} , σ , and $\mu \neq 0$).

For the power levels used in the experiment, the impact of 3PA, FCA, and FCD is not significant, as the overall spectral shape of the three plots shown in Fig.

4.4(a) are similar. The spectral gaps in the SCG are a result of the limited power output of the OPO; theoretically, an increase in pump power should result in continuous, spectrally flat SCG. However, the nonlinear loss mechanisms may become prohibitive at higher power levels. To understand the impact of these nonlinear effects more clearly, simulations are performed with the pump power is increased to 60 W, and the resulting SCG spectra are shown in Figs. 4.4(b) – 4.4(d).

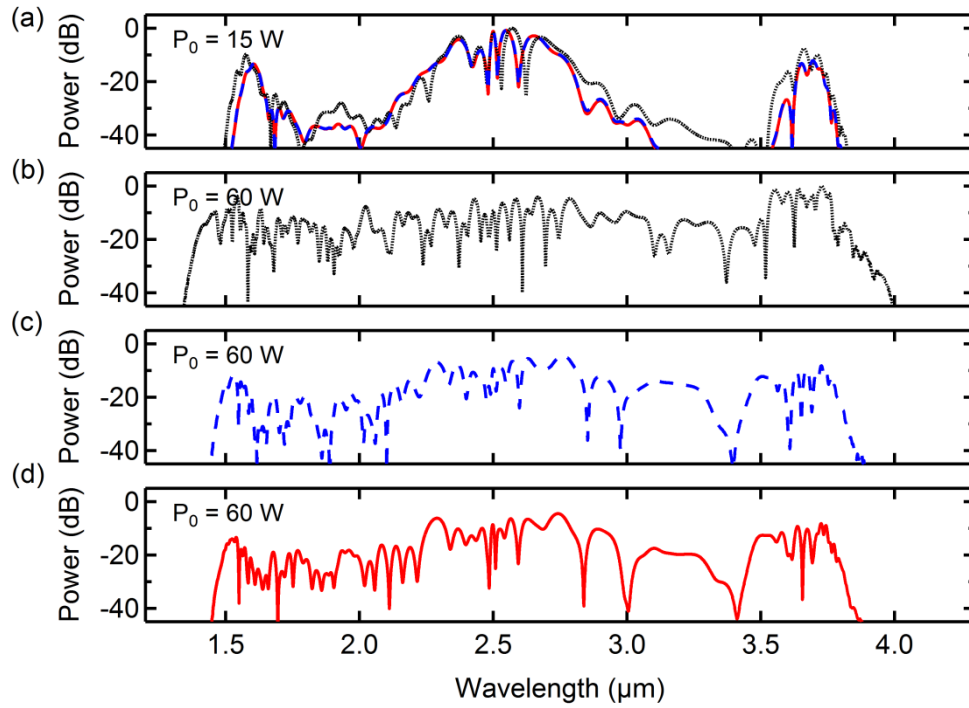


Fig. 4.4: (a) Simulated SCG output spectra from 2.5- μm pump with $P_0 = 15\text{ W}$. $\gamma_{3PA} = 0$ (black); $\gamma_{3PA} \neq 0, \sigma$ and $\mu = 0$ (blue); and γ_{3PA}, σ , and $\mu \neq 0$ (red) are shown. SCG output spectra with $P_0 = 60\text{ W}$ for (b) $\gamma_{3PA} = 0$, (c) $\gamma_{3PA} \neq 0, \sigma$ and $\mu = 0$, and (d) γ_{3PA}, σ , and $\mu \neq 0$. All plots have been normalized to the case with no nonlinear loss mechanisms (black dotted line in (b)).

We find that 3PA reduces the total optical power and narrows the spectral bandwidth, while the generated free carriers do not significantly affect the SCG process, since

they trail behind the pulse as it propagates along the nanowaveguide. We conclude that although the effect of 3PA is more pronounced at higher power levels, it is not sufficient enough to significantly inhibit broadband SCG in the regime presented here.

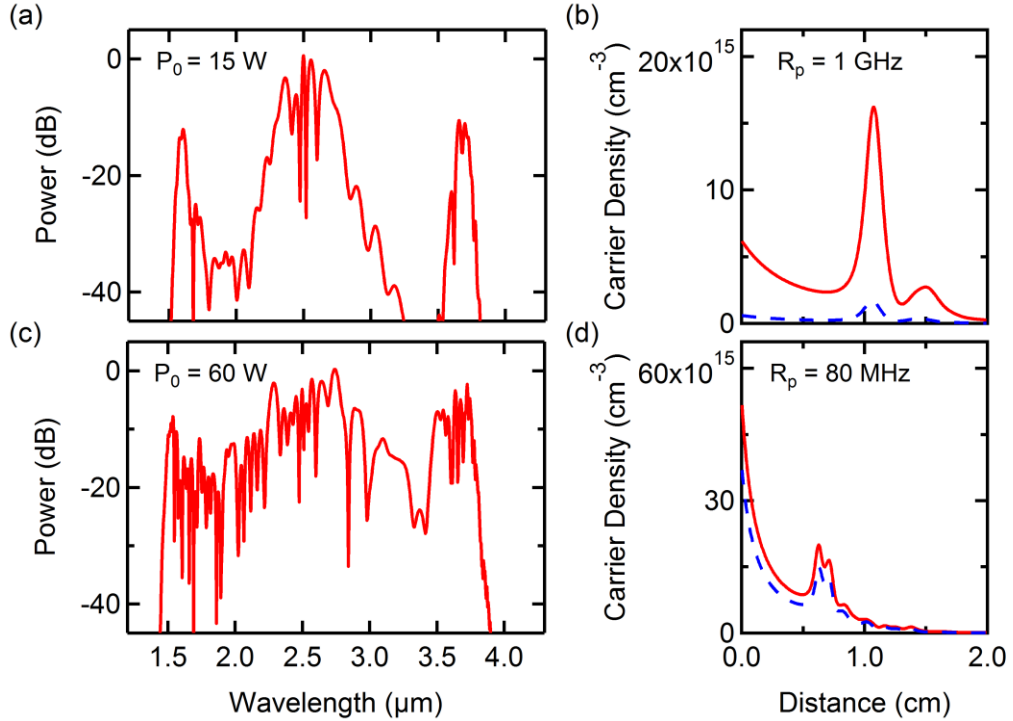


Fig. 4.5: Simulated SCG output spectra and free-carrier density along the length of the nanowaveguide after 50 consecutive pulses, using a 2.5- μ m pump with (a), (b) $P_0 = 15$ W and $R_p = 1$ GHz; and (c), (d) $P_0 = 60$ W and $R_p = 80$ MHz. Dashed blue lines show free-carrier density for a single pulse.

The preceding analysis is valid for a pulsed source with a relatively low repetition rate R_p such that the free carriers generated from a given pulse recombine before they interact with subsequent pulses via FCA ($R_p \tau_{eff} < 1$). We now consider the case in which the repetition rate is on a time scale comparable to the free-carrier lifetime. A high-repetition-rate train of 50 pulses is propagated along the 2-cm-long nanowaveguide, and the generated carriers are allowed to accumulate between pulses until a steady state is reached. Figure 4.5(a) shows the resulting SCG spectrum for

$P_0 = 15 \text{ W}$ and $R_p = 1 \text{ GHz}$ ($R_p \tau_{eff} = 10$), and Fig. 4.5(b) shows the free-carrier density along the length of the nanowaveguide. As the peak power is still relatively low, we observe that the accumulation of free carriers do not contribute significantly to FCA of subsequent pulses, even at much higher repetition rates.

We next perform simulations to analyze the nonlinear loss effects at high pump powers, using a pulse train of $P_0 = 60 \text{ W}$ and $R_p = 1 \text{ GHz}$ ($R_p \tau_{eff} = 10$). We find that the increased power results in an accumulation of free carriers which is sufficient to inhibit SCG through FCA. Therefore, in order use a high-power pump to obtain spectrally flat SCG, a low-repetition-rate source must be used. This scenario is simulated using a pulse train of $P_0 = 60 \text{ W}$ and $R_p = 80 \text{ MHz}$ ($R_p \tau_{eff} < 1$). At steady state, broadband supercontinuum is generated successfully, and the spectrum and free-carrier density are shown in Figs. 4.5(c) and (d), respectively. For the low-power, high-repetition-rate SCG, the majority of free carriers are generated halfway along the nanowaveguide, corresponding to the onset of soliton fission and maximum pulse intensity (Fig. 4.5(b)). For the high-power, low-repetition-rate SCG, the majority of free carriers are generated at the input of the nanowaveguide, as the initial intensity of the pump pulse is higher (Fig. 4.5(d)). We conclude that for a given free-carrier lifetime, there is an inherent tradeoff between pump power and repetition rate in order that must be considered to avoid detrimental FCA.

4.4 Summary

In this chapter we have reported the first demonstration of octave-spanning SCG and the longest wavelength generated from a silicon nanowaveguide. We have engineered the length and GVD of our devices to enable broadband SCG facilitated by soliton

fission and dispersive wave generation in both normal-GVD regimes. We have achieved spectra spanning from 1.5 μm to 3.6 μm , covering over 1.3 octaves. We also have performed a comprehensive analysis of 3PA and free-carrier loss mechanisms, and have concluded that they are not detrimental to SCG in the regime presented here, but will become significant for increased pump powers and repetition rates.

REFERENCES

- [1] S. A. Diddams, D. J. Jones, J. Ye, S. T. Cundiff, J. L. Hall, J. K. Ranka, R. S. Windeler, R. Holzwarth, T. Udem, and T. W. Hansch, *Phys. Rev. Lett.* **84**, 5102 (2000).
- [2] I. Hartl, X. D. Li, C. Chudoba, R. K. Ghanta, T. H. Ko, J. G. Fujimoto, J. K. Ranka, and R. S. Windeler, *Opt. Lett.* **26**, 608 (2001).
- [3] K. B. Shi, P. Li, S. Z. Yin, and Z. W. Liu, *Opt. Express* **12**, 2096 (2004).
- [4] J. K. Ranka, R. S. Windeler, and A. J. Stentz, *Opt. Lett.* **25**, 25 (2000).
- [5] A. V. Husakou and J. Herrmann, *Phys. Rev. Lett.* **87**, 4 (2001).
- [6] A. L. Gaeta, *Opt. Lett.* **27**, 924 (2002).
- [7] W. J. Wadsworth, A. Ortigosa-Blanch, J. C. Knight, T. A. Birks, T. P. M. Man, and P. S. Russell, *J. Opt. Soc. Am. B: Opt. Phys.* **19**, 2148 (2002).
- [8] G. Genty, M. Lehtonen, H. Ludvigsen, and M. Kaivola, *Opt. Express* **12**, 3471 (2004).
- [9] J. M. Dudley, G. Genty, and S. Coen, *Rev. Mod. Phys.* **78**, 1135 (2006).
- [10] M. R. E. Lamont, B. Luther-Davies, D. Y. Choi, S. Madden, and B. J. Eggleton, *Opt. Express* **16**, 14938 (2008).
- [11] N. Granzow, S. P. Stark, M. A. Schmidt, A. S. Tverjanovich, L. Wondraczek, and P. S. J. Russell, *Opt. Express* **19**, 21003 (2011).
- [12] D. Duchesne, M. Peccianti, M. R. E. Lamont, M. Ferrera, L. Razzari, F. Legare, R. Morandotti, S. Chu, B. E. Little, and D. J. Moss, *Opt. Express* **18**, 923 (2010).
- [13] R. Halir, Y. Okawachi, J. S. Levy, M. A. Foster, M. Lipson, and A. L. Gaeta, *Opt. Lett.* **37**, 1685 (2012).
- [14] I. W. Hsieh, X. G. Chen, X. P. Liu, J. I. Dadap, N. C. Panoiu, C. Y. Chou, F. N. Xia, W. M. Green, Y. A. Vlasov, and R. M. Osgood, *Opt. Express* **15**, 15242 (2007).
- [15] B. Kuyken, X. P. Liu, R. M. Osgood, R. Baets, G. Roelkens, and W. M. J. Green, *Opt. Express* **19**, 20172 (2011).
- [16] U. D. Dave, S. Uvin, B. Kuyken, S. Selvaraja, F. Leo, and G. Roelkens, *Opt. Express* **21**, 32032 (2013).

- [17] G. Agrawal, *Nonlinear Fiber Optics* (Academic Press, 2006).
- [18] L. H. Yin, and G. P. Agrawal, *Opt. Lett.* **32**, 2031 (2007).
- [19] L. H. Yin, Q. Lin, and G. P. Agrawal, *Opt. Lett.* **32**, 391 (2007).
- [20] R. Claps, V. Raghunathan, D. Dimitropoulos, and B. Jalali, *Opt. Express* **12**, 2774 (2004).
- [21] R. A. Soref and B. R. Bennett, *IEEE J. Quant. Electron.* **23**, 123 (1987).
- [22] F. Gholami, S. Zlatanovic, A. Simic, L. Liu, D. Borlaug, N. Alic, M. P. Nezhad, Y. Fainman, and S. Radic, *Appl. Phys. Lett.* **99**, 3 (2011).
- [23] S. Pearl, N. Rotenberg, and H. M. van Driel, *Appl. Phys. Lett.* **93**, 3 (2008).
- [24] A. C. Turner-Foster, M. A. Foster, J. S. Levy, C. B. Poitras, R. Salem, A. L. Gaeta, and M. Lipson, *Opt. Express* **18**, 3582 (2010).
- [25] R. K. W. Lau, M. Menard, Y. Okawachi, M. A. Foster, A. C. Turner-Foster, R. Salem, M. Lipson, and A. L. Gaeta, *Opt. Lett.* **36**, 1263 (2011).

CHAPTER 5

MICRORESONATOR-BASED PARAMETRIC COMB GENERATION

Optical frequency combs (OFCs) are characterized by discrete, regularly spaced narrow lines in the frequency domain. There is great interest in stable combs with broad bandwidths for applications which include optical clocks, frequency metrology, and high-precision spectroscopy [1]. One promising approach to generating OFCs arises from parametric mixing in high-Q microresonators. Such microresonators enable efficient nonlinear optical processes, which can lead to parametric oscillation and the generation of a broad range of new wavelengths from a single-frequency laser [2]. Parametric OFC generation was first observed in silica microtoroids [3], and since then has been demonstrated in silica microspheres [4], CaF_2 [5], MgF_2 [6, 7], and quartz [8] resonators, silica disks [9], high-index silica-glass microrings [10], diamond [11], aluminum nitride [12], silicon nitride [7, 13-15] and most recently, silicon [16]. The nonlinear dynamics of such microresonator-based frequency combs are complex, and simulation of the process over broad bandwidths using a modal expansion approach is computationally intensive [17, 18]. Researchers have recently applied a numerical approach based on a modified expansion of the LL model [19-23], enabling the modeling of the complete spectral-temporal dynamics of ultrabroadband frequency combs generated in silicon nitride microresonators [24].

Silicon is highly advantageous as a photonic platform for parametric oscillation, since it exhibits a large material nonlinearity and is transparent over a significant portion of the telecom and MIR regions, as discussed in Chapter 1. The devices modeled are silicon channel waveguides with either an SiO_2 or air cladding, which contributes to a large index contrast and significant waveguide dispersion,

shown to be key in optimizing broadband parametric oscillation [24]. Despite these advantages, multiphoton absorption at telecom and MIR wavelengths can significantly limit the efficiency of parametric oscillation. While the effects of multiphoton absorption have been studied in the context of Raman amplification [25, 26], SPM [27, 28], optical parametric amplification [29], and SCG [30, 31], its role in parametric comb generation has not been investigated thus far. In this chapter⁶, we present an investigation of silicon microresonator-based frequency combs using an LL model modified to include multiphoton absorption and free-carrier effects, and discuss the implications of operating in the telecom and MIR wavelength ranges. In addition, we identify regimes in the MIR in which silicon microresonator-based broadband parametric oscillation may be achieved.

5.1 Modified Lugiato-Lefever model

We introduce the modified LL equation by including contributions from higher-order dispersion, self-steepening, multiphoton absorption, and free-carrier effects, such that

$$\begin{aligned}
T_R \frac{\partial E(t, \tau)}{\partial t} = & \sqrt{\kappa} E_{in} \\
& + \left[-\frac{\alpha}{2} + \frac{\kappa}{2} - i\delta_0 + iL \sum_{k \geq 2} \frac{\beta_k}{k!} \left(i \frac{\partial}{\partial \tau} \right)^k \right. \\
& + \left(1 + \frac{i}{\omega_0} \frac{\partial}{\partial \tau} \right) \left(i\gamma L |E(t, \tau)|^2 - \frac{\beta_{2PAL}}{2A_{eff}} |E(t, \tau)|^2 \right. \\
& - \frac{\beta_{3PAL}}{2A_{eff}^2} |E(t, \tau)|^4 - \frac{\beta_{4PAL}}{2A_{eff}^3} |E(t, \tau)|^6 \left. \right) \\
& \left. - \frac{\sigma L}{2} (1 + i\mu) N_c \right] E(t, \tau), \tag{5.1}
\end{aligned}$$

⁶ R. K. W. Lau, M. R. E. Lamont, Y. Okawachi, and A. L. Gaeta, *Opt. Lett.* (Submitted 2014).

where $E(t, \tau)$ is the field within the microresonator; E_{in} is the input field at frequency ω_0 ; t and τ correspond to the time evolution of the field and the temporal field within the cavity, respectively; T_R is the round-trip time; κ is the power transmission coefficient; α is the round-trip loss; δ_0 is the cavity detuning; L is the cavity length; β_k is the k -th order dispersion coefficient; γ is the nonlinear parameter; β_{2PA} , β_{3PA} , and β_{4PA} are the 2PA, 3PA, and 4PA coefficients of silicon, respectively; A_{eff} is the effective area of the nanowaveguide mode; and σ and μ are the FCA cross section and FCD parameter, respectively [26, 32]. The free-carrier density N_c is governed by the following rate equation:

$$\frac{\partial N_c(t, \tau)}{\partial \tau} = \frac{\beta_{2PA}}{2\hbar\omega_0} \frac{|E(t, \tau)|^4}{A_{eff}^2} + \frac{\beta_{3PA}}{3\hbar\omega_0} \frac{|E(t, \tau)|^6}{A_{eff}^3} + \frac{\beta_{4PA}}{4\hbar\omega_0} \frac{|E(t, \tau)|^8}{A_{eff}^4} - \frac{N_c(t, \tau)}{\tau_{eff}}, \quad (5.2)$$

with carrier generation rates determined by multiphoton absorption, and the recombination rate determined by the effective free-carrier lifetime τ_{eff} .

Many applications of frequency combs required that the combs be mode locked, such that a single soliton pulse is generated within the microresonator, and that there exists a fixed phased relationship among the comb modes, resulting in an identical spacing between adjacent comb lines [18, 21, 23, 33]. The numerical modeling of this low-noise, mode-locked state can be achieved through a series of discrete detunings of the pump from the cavity resonance, as described in Ref. [24] (Fig. 5.1).

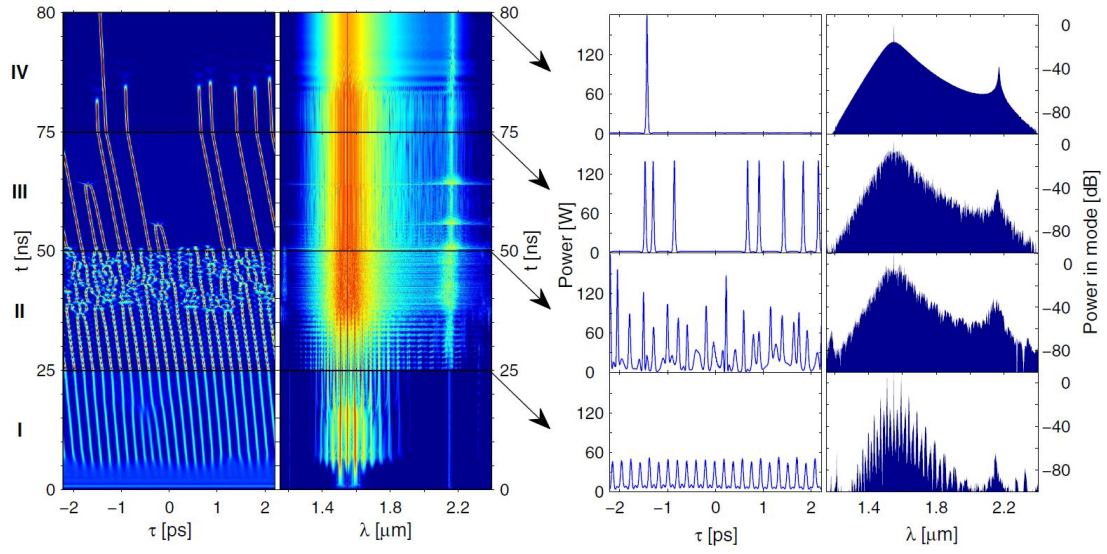


Fig. 5.1: Evolution of single-pulse modelocking for Si_3N_4 microresonator [okawachi] showing four distinct stages (Stages I – IV) in which the pump wavelength is tuned away from the cavity resonance. The temporal and spectral evolution are shown in the first and second column, respectively. The temporal and spectral power at the end of each stage are shown in the third and fourth column, respectively. Figures taken from Lamont et al. [24].

Figure 5.1 shows the temporal and spectral evolution of a Si_3N_4 microresonator-based frequency comb during the single-pulse, modelocking process. Device and simulation parameters are taken from Okawachi et al. and Lamont et al. [24], respectively. The pump wavelength is initially set to the cavity resonance, and in each of the subsequent stages, the pump is detuned away from resonance, resulting in several distinct stages of behavior. In Stage I, multiple stable cavity solitons are formed. In Stage II, the pump is tuned into to the Kerr-shifted resonance, and with the increased intracavity power, the cavity solitons become unstable and chaotic. In Stage III, the pump is detuned past the Kerr-shifted resonance, and with the decreased intracavity power, multiple stable cavity solitons reform. Finally, in Stage IV, the pump is further detuned and the multiple solitons begin to dissipate until a single pulse remains within the microresonator.

5.2 Parametric oscillation in telecom and mid-infrared regimes

We first consider a microresonator engineered for parametric oscillation in the telecom range, pumped with 1 W of CW power at 1.56 μm . The device is modeled after the SiO_2 -clad silicon nanowaveguides presented in Ref. [34], and its properties are summarized in Table 5.1 along with other simulation parameters. Spectra generated in the absence (blue) and presence (red) of 2PA are shown in Fig. 5.2(b). It is clear that in the telecom regime, the inclusion of nonlinear loss significantly inhibits parametric oscillation. We note that the process of 2PA itself is sufficient to inhibit oscillation, as simulations which include 2PA without free-carrier effects yield similar results.

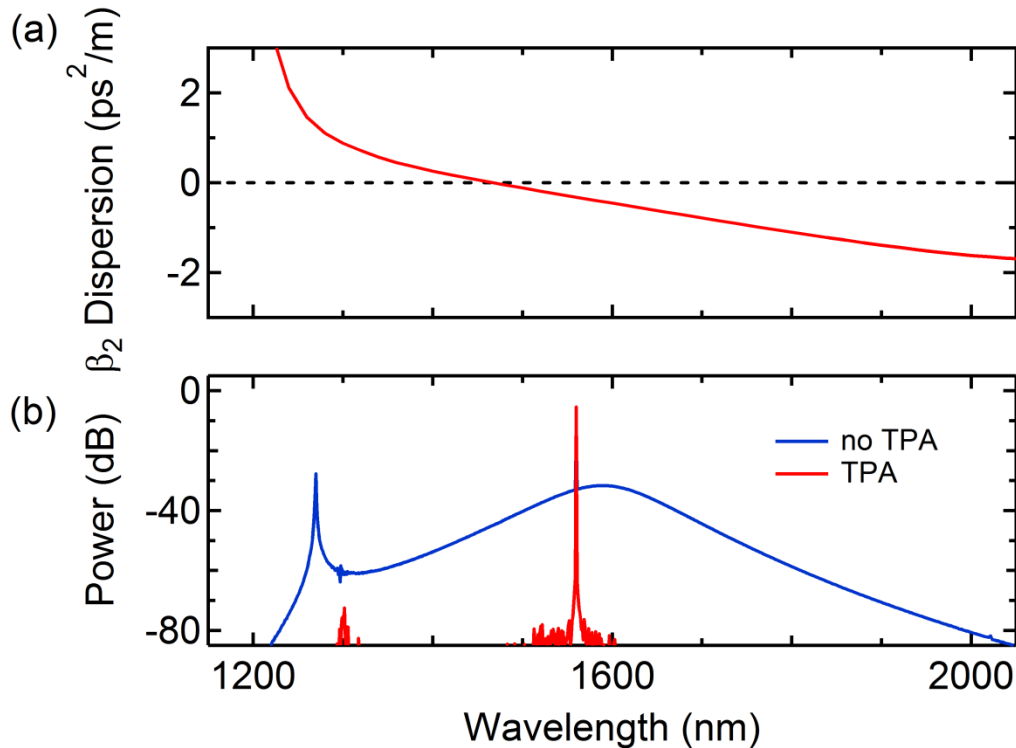


Fig. 5.2: (a) GVD and (b) OFC spectra for silicon microresonator engineered for parametric oscillation in the telecom regime. Spectra are generated in the absence (blue) and presence (red) of 2PA using 1 W of pump power at 1.56 μm .

| | | | |
|---|------------------------|------------------------|------------------------|
| Pump Wavelength (μm) | 1.56 | 2.4 | 4.0 |
| Pump Power (W) | 1 | 1 | 0.35 |
| Waveguide Area (nm^2) | 690 x 300 | 1400 x 500 | 2600 x 500 |
| Cladding Material | SiO_2 | SiO_2 | Air |
| Resonator Radius (μm) | 100 | 100 | 100 |
| Propagation Loss (dB/cm) | 1.4 | 0.7 | 0.7 |
| n_2 (cm^2/W) | 4×10^{-14} | 7×10^{-14} | 3×10^{-14} |
| β_{2PA} (cm/GW) | 1.5 | - | - |
| β_{3PA} (cm^3/GW^2) | - | 0.02 | - |
| β_{4PA} (cm^5/GW^3) | - | - | 3×10^{-5} |
| σ (m^2) | 1.47×10^{-21} | 3.48×10^{-21} | 9.67×10^{-21} |
| μ | 7.5 | 4.9 | 2.9 |
| τ_{eff} (ns) | 3 | 5 | 5 |

Table 5.1: Simulation values for microresonator parameters and material properties over telecom and MIR wavelengths. Values for n_2 , β , and τ_{eff} , as well as expressions for σ and μ are taken from literature [16, 30, 32, 34-37].

Consequently, reducing nonlinear loss is essential to frequency comb generation, and indeed significant process has been made in this direction in a recent demonstration of silicon microresonator-based parametric oscillation at MIR wavelengths [16]. In this next section, we consider an SiO_2 -clad, etchless silicon device similar to that used in Ref. [16], pumped with 1 W of CW power at 2.4 μm , where 3PA becomes the dominant nonlinear absorption process. Device parameters and material properties for simulation are summarized in Table 5.1. The spectra generated in the absence of 3PA (blue), presence of 3PA without free carriers (green), and presence of 3PA and free carriers (red) are shown in Fig. 5.3(b). We observe once again that oscillation does not occur when all the nonlinear loss terms are included.

Interestingly, in contrast to the telecom regime, it is evident that the limiting mechanism in this case is the FCA, and not the 3PA, as simulations which include 3PA without free carriers (green) are similar to those without any nonlinear loss terms (blue).

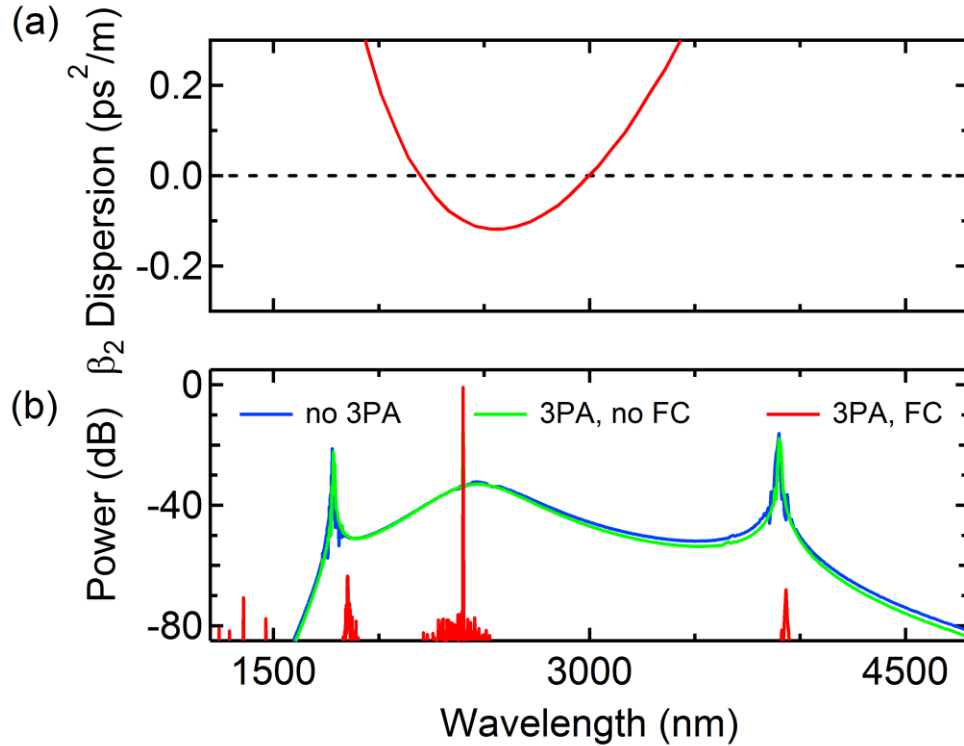


Fig. 5.3: (a) GVD and (b) OFC spectra for etchless silicon microresonator engineered for parametric oscillation in the MIR regime. Spectra are generated in the absence of 3PA (blue), presence of 3PA with no free carriers (green), and presence of 3PA and free carriers (red) using 1 W of pump power at 2.4 μ m.

Since the rate of free carrier generation is intensity dependent, one approach to mitigating FCA is simply to lower the pump power and reduce the on-chip optical intensity. By reducing the pump power from 1 W to 10 mW, a frequency comb can be generated with a 2.4- μ m pump, despite the presence of 3PA and FCA. The spectrum, temporal profile, and free-carrier density within the microresonator are shown in Fig.

5.4(a), (b), and (c), respectively. However, this approach limits the achievable parametric bandwidth and is not conducive to generating a broadband frequency comb.

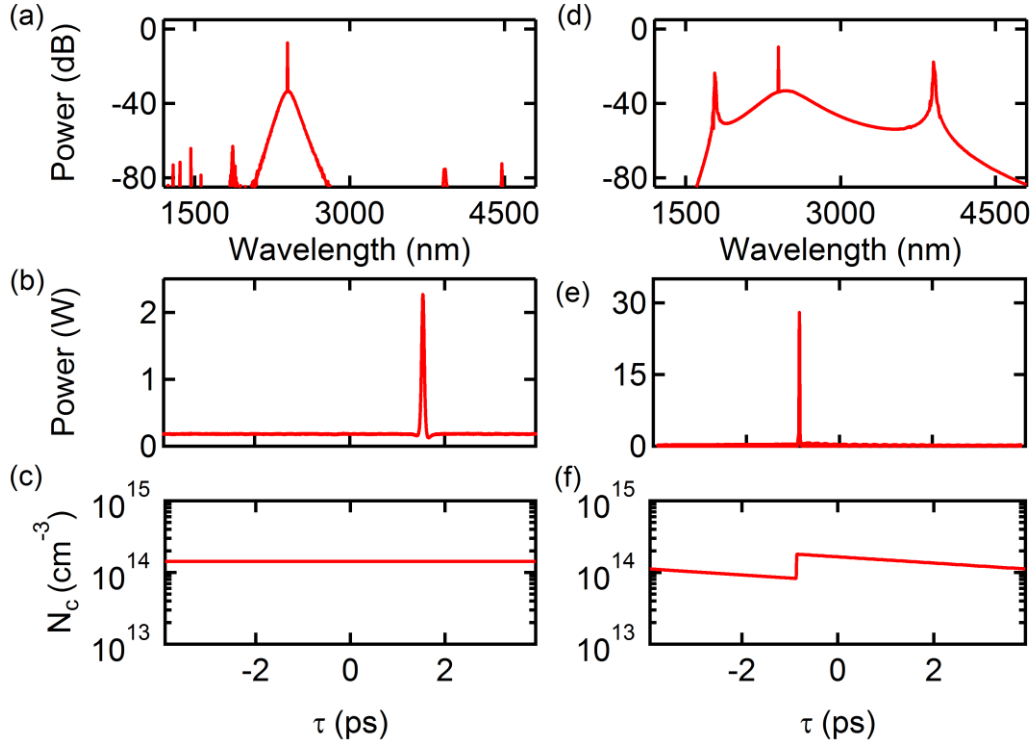


Fig. 5.4: (a) Spectrum, (b) temporal profile, and (c) free-carrier density for microresonator pumped with 10 mW of pump power at 2.4 μm in presence of 3PA with $\tau_{eff} = 5$ ns. (d) Spectrum, (e) temporal profile, and (f) free-carrier density for microresonator pumped with 1 W of pump power at 2.4 μm in presence of 3PA with $\tau_{eff} = 10$ ps.

We can understand the role that free carriers have on comb generation by examining the time-dependent carrier behavior within the microresonator. In Fig. 5.4(c), we observe that the free-carrier density has build up to a constant value throughout the cavity, as the intrinsic free-carrier lifetime of 5 ns is much longer than the cavity round-trip time of 6 ps. A more promising approach is to lower the free-

carrier density within the microresonator by reducing the effective free-carrier lifetime, which can be done, for example, using an integrated $p-i-n$ diode [37-41]. Turner-Foster et al. have demonstrated a free-carrier lifetime of 12.2 ps in silicon nanowaveguides by applying a reverse bias across an integrated $p-i-n$ diode (Fig. 5.5) [37].

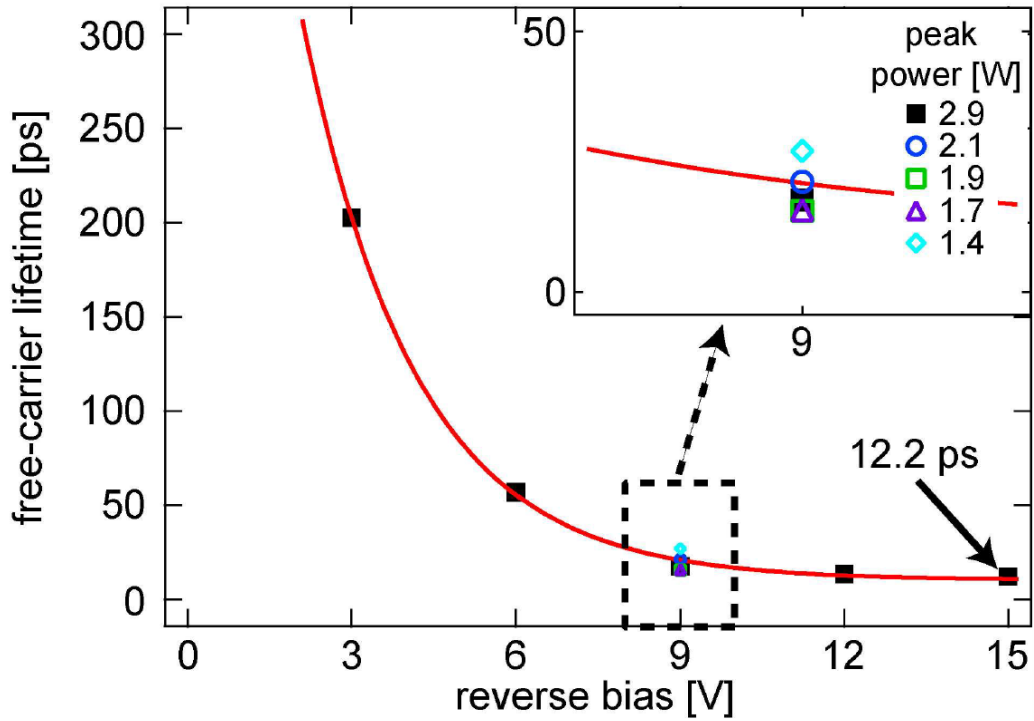


Fig. 5.5: Measured free-carrier lifetime as a function of reverse bias, showing a reduction of free-carrier lifetime from the intrinsic value of 3 ns to 12.2 ps. Figure taken from Turner-Foster et al. [37].

With the free-carrier lifetime reduced to 10 ps, a broadband frequency comb can be generated with 1 W of pump power in the presence of 3PA and FCA. The resulting spectrum and temporal profile are shown in Fig. 5.4(d) and (e), respectively, and are representative of a single-pulse, mode-locked state. The spectral bandwidth exceeds an octave, and the peak power of the circulating soliton pulse is much higher,

as compared to Figs. 5.4(a) and (b). The effective free-carrier lifetime of 10 ps is on the same time scale as the round-trip cavity time, and an appreciable decay of the carrier density is observed within the microresonator in Fig. 5.4(f). We note that although the peak power is much higher, the magnitude of the free-carrier density is still comparable to that of the 10-mW comb because of the reduced free-carrier lifetime.

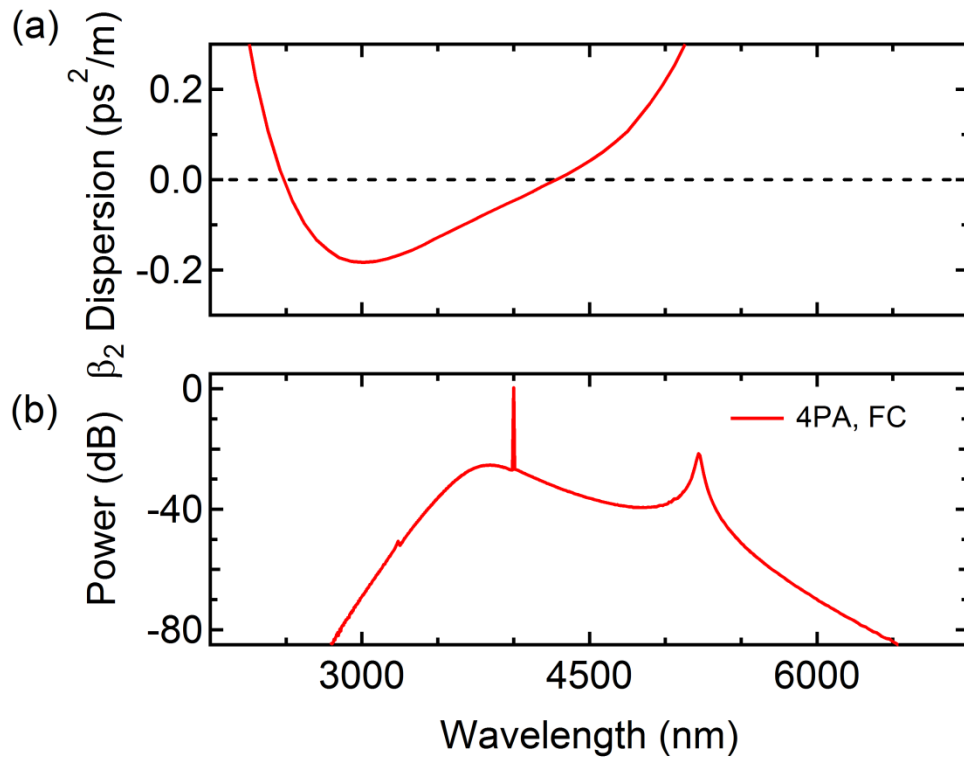


Fig. 5.6: (a) GVD and (b) OFC spectrum for etchless air-clad silicon microresonator engineered for parametric oscillation in the MIR regime. Spectrum is generated in the presence of 4PA and free carriers using 350 mW of pump power at 4.0 μm .

Moving to longer MIR wavelengths beyond 3.3 μm reduces the nonlinear loss even further. Although the material nonlinearity n_2 is lower in this wavelength range, there exists a key advantage due to the lack of 2PA or 3PA, since the dominant

nonlinear absorption process is 4PA. However, since the SiO₂ cladding in the previous analysis introduces significant absorption loss at these wavelengths, we consider an air-clad, etchless silicon microresonator pumped at 4 μm [16]. Device and simulation parameters are summarized in Table 5.1. We observe behavior similar to that above, in which either the pump power or effective free-carrier lifetime must be sufficiently low in order to avoid excessive FCA. This condition is not as strict, since the rate of carrier generation due to 4PA is lower than that due to 3PA. In fact, a moderate pump power of 350 mW avoids detrimental FCA, yet still results in broad parametric bandwidth, as shown by the frequency comb spectrum in Fig. 5.6(b). By operating in this regime, mode-locked, octave-spanning frequency combs can be generated in passive microresonator structures, eliminating the need for the complex integration of *p-i-n* structures.

5.3 Summary

In this chapter we have presented numerical simulation to analyze parametric frequency comb generation in silicon microresonators in the presence of multiphoton absorption and free-carrier effects using a modified LL equation. We have investigated the impact of 2PA, 3PA, 4PA, FCA, and FCD over several different wavelength ranges. We find that at telecom wavelengths, 2PA is sufficient to inhibit parametric oscillation and comb generation. At MIR wavelengths where 3PA is dominant, we can observe a frequency comb despite the presence of 3PA and FCA, provided that the pump power is sufficiently low or the free-carrier lifetime is made sufficiently short. At longer wavelengths where 4PA is dominant, we observe generation of an octave-spanning frequency comb at moderate pump powers of several hundred mW without needing to reduce the free-carrier lifetime. The modeling and

analysis presented here have been instrumental in achieving the first demonstration of optical parametric oscillation in a silicon microresonator [16].

REFERENCES

- [1] T. Udem, R. Holzwarth, and T. W. Hansch, *Nature* **416**, 233 (2002).
- [2] T. J. Kippenberg, S. M. Spillane, and K. J. Vahala, *Phys. Rev. Lett.* **93**, 4 (2004).
- [3] P. Del'Haye, A. Schliesser, O. Arcizet, T. Wilken, R. Holzwarth, and T. J. Kippenberg, *Nature* **450**, 1214 (2007).
- [4] I. H. Agha, Y. Okawachi, and A. L. Gaeta, *Opt. Express* **17**, 16209 (2009).
- [5] A. A. Savchenkov, A. B. Matsko, W. Liang, V. S. Ilchenko, D. Seidel, and L. Maleki, *Opt. Express* **20**, 27290 (2012).
- [6] W. Liang, A. A. Savchenkov, A. B. Matsko, V. S. Ilchenko, D. Seidel, and L. Maleki, *Opt. Lett.* **36**, 2290 (2011).
- [7] T. Herr, K. Hartinger, J. Riemensberger, C. Y. Wang, E. Gavartin, R. Holzwarth, M. L. Gorodetsky, and T. J. Kippenberg, *Nature Photon.* **6**, 480 (2012).
- [8] S. B. Papp and S. A. Diddams, *Phys. Rev. A* **84**, 7 (2011).
- [9] J. Li, H. Lee, T. Chen, and K. J. Vahala, *Phys. Rev. Lett.* **109**, 5 (2012).
- [10] L. Razzari, D. Duchesne, M. Ferrera, R. Morandotti, S. Chu, B. E. Little, and D. J. Moss, *Nature Photon.* **4**, 41 (2010).
- [11] B. J. M. Hausmann, I. Bulu, V. Venkataraman, P. Deotare, and M. Loncar, *Nature Photon.* **8**, 369 (2014).
- [12] H. Jung, C. Xiong, K. Y. Fong, X. F. Zhang, and H. X. Tang, *Opt. Lett.* **38**, 2810 (2013).
- [13] J. S. Levy, A. Gondarenko, M. A. Foster, A. C. Turner-Foster, A. L. Gaeta, and M. Lipson, *Nature Photon.* **4**, 37 (2010).
- [14] M. A. Foster, J. S. Levy, O. Kuzucu, K. Saha, M. Lipson, and A. L. Gaeta, *Opt. Express* **19**, 14233 (2011).
- [15] F. Ferdous, H. X. Miao, D. E. Leaird, K. Srinivasan, J. Wang, L. Chen, L. T. Varghese, and A. M. Weiner, *Nature Photon.* **5**, 770 (2011).
- [16] A. G. Griffith, R. K. W. Lau, J. Cardenas, Y. Okawachi, A. Mohanty, R. Fain, Y. H. D. Lee, M. Yu, C. T. Phare, C. B. Poitras, A. L. Gaeta, and M. Lipson, *arXiv:1408.1039* (2014).

- [17] Y. K. Chembo and N. Yu, *Phys. Rev. A* **82**, 18 (2010).
- [18] T. Herr, V. Brasch, J. D. Jost, C. Y. Wang, N. M. Kondratiev, M. L. Gorodetsky, and T. J. Kippenberg, *Nature Photon.* **8**, 145 (2014).
- [19] L. A. Lugiato and R. Lefever, *Phys. Rev. Lett.* **58**, 2209 (1987).
- [20] M. Haelterman, S. Trillo, and S. Wabnitz, *Opt. Comm.* **91**, 401 (1992).
- [21] A. B. Matsko, A. A. Savchenkov, W. Liang, V. S. Ilchenko, D. Seidel, and L. Maleki, *Opt. Lett.* **36**, 2845 (2011).
- [22] S. Coen, H. G. Randle, T. Sylvestre, and M. Erkintalo, *Opt. Lett.* **38**, 37 (2013).
- [23] Y. K. Chembo and C. R. Menyuk, *Phys. Rev. A* **87**, 4 (2013).
- [24] M. R. E. Lamont, Y. Okawachi, and A. L. Gaeta, *Opt. Lett.* **38**, 3478 (2013).
- [25] T. K. Liang and H. K. Tsang, *Appl. Phys. Lett.* **84**, 2745 (2004).
- [26] R. Claps, V. Raghunathan, D. Dimitropoulos, and B. Jalali, *Opt. Express* **12**, 2774 (2004).
- [27] L. H. Yin and G. P. Agrawal, *Opt. Lett.* **32**, 2031 (2007).
- [28] Y. Liu and H. K. Tsang, *Appl. Phys. Lett.* **90**, 3 (2007).
- [29] X. P. Liu, R. M. Osgood, Y. A. Vlasov, and W. M. J. Green, *Nature Photon.* **4**, 557 (2010).
- [30] X. Gai, Y. Yu, B. Kuyken, P. Ma, S. J. Madden, J. Van Campenhout, P. Verheyen, G. Roelkens, R. Baets, and B. Luther-Davies, *Laser Photon. Rev.* **7**, 1054 (2013).
- [31] L. H. Yin, Q. Lin, and G. P. Agrawal, *Opt. Lett.* **32**, 391 (2007).
- [32] R. A. Soref and B. R. Bennett, *IEEE J. Quant. Electron.* **23**, 123 (1987).
- [33] K. Saha, Y. Okawachi, B. Shim, J. S. Levy, R. Salem, A. R. Johnson, M. A. Foster, M. R. E. Lamont, M. Lipson, and A. L. Gaeta, *Opt. Express* **21**, 1335 (2013).
- [34] A. C. Turner, C. Manolatou, B. S. Schmidt, M. Lipson, M. A. Foster, J. E. Sharping, and A. L. Gaeta, *Opt. Express* **14**, 4357 (2006).
- [35] A. D. Bristow, N. Rotenberg, and H. M. van Driel, *Appl. Phys. Lett.* **90**, 3 (2007).

- [36] S. Pearl, N. Rotenberg, and H. M. van Driel, *Appl. Phys. Lett.* **93**, 3 (2008).
- [37] A. C. Turner-Foster, M. A. Foster, J. S. Levy, C. B. Poitras, R. Salem, A. L. Gaeta, and M. Lipson, *Opt. Express* **18**, 3582 (2010).
- [38] R. Jones, H. S. Rong, A. S. Liu, A. W. Fang, M. J. Paniccia, D. Hak, and O. Cohen, *Opt. Express* **13**, 519 (2005).
- [39] H. S. Rong, R. Jones, A. S. Liu, O. Cohen, D. Hak, A. Fang, and M. Paniccia, *Nature* **433**, 725 (2005).
- [40] S. R. Preble, Q. F. Xu, B. S. Schmidt, and M. Lipson, *Opt. Lett.* **30**, 2891 (2005).
- [41] Y. H. Kuo, H. S. Rong, V. Sih, S. B. Xu, M. Paniccia, and O. Cohen, *Opt. Express* **14**, 11721 (2006).

CHAPTER 6

SILICON-NITRIDE-CLAD NANOWAVEGUIDES

Silicon has been established as a promising material for nonlinear photonics in the MIR due to its high refractive index, large nonlinearity, and transparency, but for wavelengths beyond 3 μm , alternative materials must be considered due to the absorption of the SiO_2 cladding used in standard SOI waveguides [1, 2]. In this chapter⁷, we introduce a novel waveguiding platform which uses standard SOI wafers, but has a top cladding of silicon nitride, transparent up to 6.6 μm . We design, fabricate, and characterize these nanowaveguides and demonstrate the potential of this platform by showing broadband FWM near 2 μm .

6.1 Nanowaveguide design, fabrication, and characterization

A schematic cross section of the Si_3N_4 -clad nanowaveguide is shown in Fig. 6.1(a). In comparison to the standard SiO_2 -clad devices presented in previous chapters, here the only interaction between the waveguide mode and the SiO_2 cladding is at the bottom interface, reducing the overall loss due to material absorption from the SiO_2 . Additionally, the higher refractive index of the silicon nitride further reduces this interaction, as the mode is preferentially located in the higher index region. Figure 6.1(b) shows the simulated GVD for the fundamental TE mode for nanowaveguides of varying widths and a height of 500 nm. We find that a cross section of 1360 nm by 500 nm is optimum for our pump wavelength near 2.2 μm .

⁷ R. K. W. Lau, M. Ménard, Y. Okawachi, M. Lipson, and A. L. Gaeta, Conference on Lasers and Electro-Optics: 2013, (Optical Society of America, 2013), paper CM1L.5.

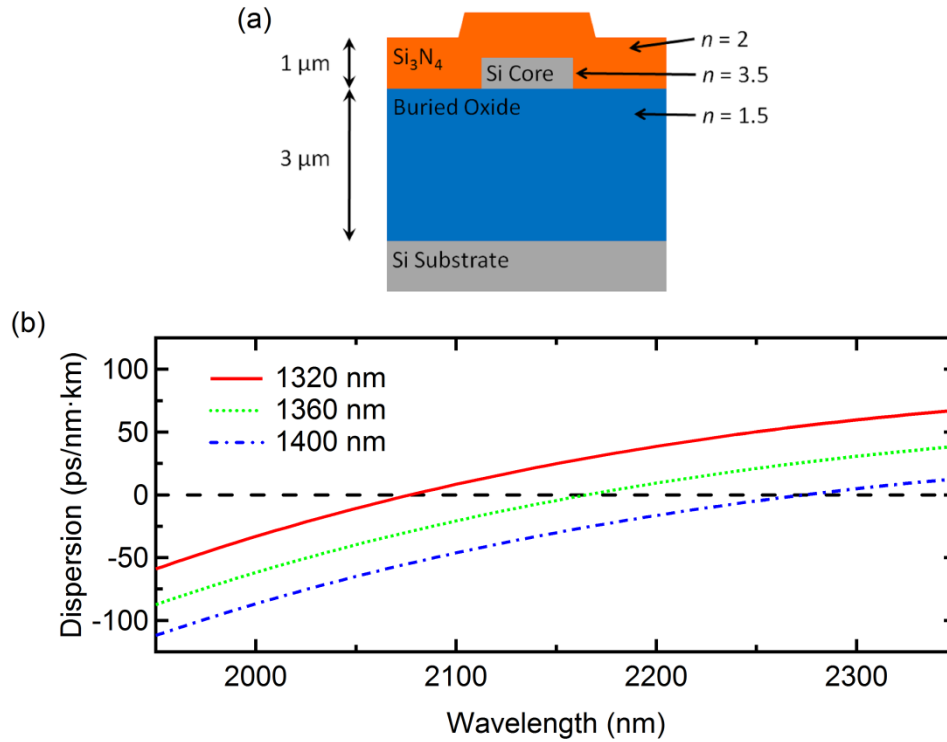


Fig. 6.1: (a) Cross section schematic of Si₃N₄-clad SOI nanowaveguide. (b) Simulated GVD for the TE mode of nanowaveguides with widths ranging from 1320 nm to 1400 nm and a height of 500 nm.

The nanowaveguides are fabricated⁸ on SOI wafers and patterned using electron beam lithography with a 500-nm-thick silicon layer and 3 μm of buried oxide. The waveguides are then dry etched with an SF₆ chemistry, and the remaining resist is removed via an oxygen plasma. A 1-μm-thick layer of Si₃N₄ is deposited on top of the waveguides using PECVD.

Upon polishing the chip edges, we observed that the deposited Si₃N₄ did not bond well to the buried oxide layer, resulting in delamination of the top cladding (Fig. 6.2(a)). To overcome this issue, an additional layer of SiO₂ is added. Si₃N₄ away from the silicon core is removed using photolithography and dry etching, and a 3-μm layer

⁸ Fabrication done by Dr. Michaël Ménard in Professor Michal Lipson's group at Cornell University.

of PECVD SiO_2 is deposited. A schematic cross section of the modified nanowaveguide design is shown in Fig. 6.2(b). We note that the oxide overcladding is located far away from the silicon core and thus does not interact with the waveguide mode. Figure 6.3(c) is an image of the top view of the completed chip, showing the Si_3N_4 -clad region over the spiral layout of the nanowaveguides and clean input tapers. Once fabrication is complete, we use the cut-back method [3] to characterize the coupling and propagation losses of the nanowaveguides to be 5 dB/facet and 5 dB/cm, respectively, at the pump wavelength of 2.2 μm .

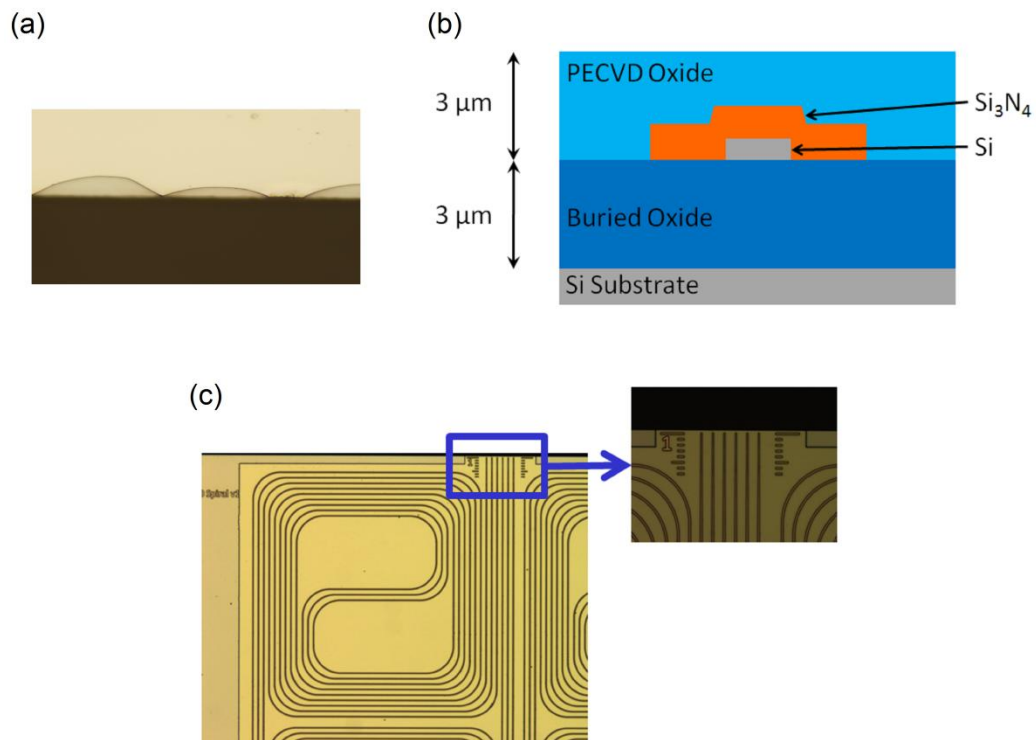


Fig. 6.2: (a) Side view of chip edge showing delamination of Si_3N_4 cladding at interface between Si_3N_4 and SiO_2 (b) Schematic cross section of nanowaveguide with deposited SiO_2 overcladding (c) Top view of chip after additional SiO_2 overcladding process. Input tapers for six nanowaveguides shown in inset.

6.2 Four-wave mixing at mid-infrared wavelengths

In the FWM experiments, the nanowaveguide cross section is 1360 nm wide by 500 nm tall, and the devices are 1 cm long. The pump and signal sources are two high power $\text{Cr}^{2+}:\text{ZnSe}$ lasers in a configuration similar to that described in Chapter 3. Figure 6.3(a) shows the measured FWM spectra as the signal wavelength is tuned from 2193 nm to 2336 nm. Wavelength conversion is achieved over 300 nm, from 2336 nm to 2029 nm. The peak CE is -33 dB and varies less than 3 dB over this entire range, while the observable parametric bandwidth of 300 nm is limited only by the OSA detection limit of 2.4 μm .

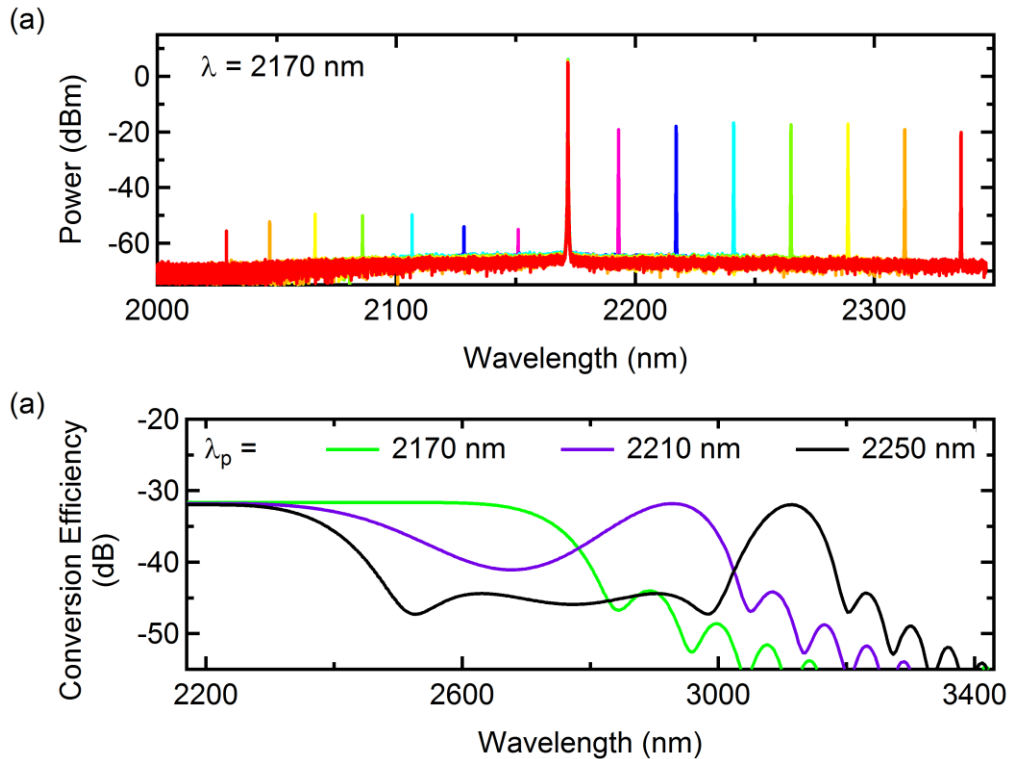


Fig. 6.3 (a) FWM spectra with 2170-nm pump and signal tuned from 2193 nm to 2336 nm. Measured conversion efficiency ranges from -33 dB to -35 dB over 300 nm. (b) Theoretical conversion efficiency showing discrete phase matching bands for pump wavelengths of 2170 nm, 2210 nm, and 2250 nm.

The FWM process is modeled by numerical integration of the coupled differential equations presented in Chapter 3, and the theoretical conversion efficiency is presented as a function of idler wavelength in Fig 6.3(b). For the waveguide dimensions and 2170-nm pump presented here, the predicted 3-dB conversion bandwidth is approximately 945 nm, corresponding to an idler wavelength of 2741 nm (green). The continuous parametric bandwidth is limited by the phase matching condition discussed in Section 3.1. It has been shown that the presence of higher-order dispersion enables phase matching at discrete wavelength bands far away from the pump [4-6]. We observe that longer wavelengths beyond 3 μm can be reached as the pump is tuned to longer wavelengths (purple, black). Furthermore, these devices may be designed to operate at even longer MIR pump wavelengths by tailoring the waveguide dimensions to position the ZGVD wavelength further in the MIR.

6.3 Summary

In this chapter we have designed, fabricated, and characterized silicon nanowaveguides with an Si_3N_4 top cladding, engineered for operation at MIR wavelengths where SiO_2 absorption becomes prohibitive. We achieve broadband FWM using a CW pump near 2 μm and measure a 3-dB parametric bandwidth greater than 300 nm with a peak conversion efficiency of -33 dB. These results represent the first demonstration of wavelength conversion on a novel Si_3N_4 -clad SOI platform and show promise in generating much longer MIR wavelengths via FWM while maintaining a relatively straightforward CMOS-compatible fabrication process.

REFERENCES

- [1] R. Soref, *Nature Photon.* **4**, 495-497 (2010).
- [2] R. A. Soref, S. J. Emelett, and A. R. Buchwald, *J. Opt. A: Pure Appl. Opt.* **8**, 840 (2006).
- [3] G. T. Reed and A. P. Knights, *Silicon Photonics: An Introduction* (Wiley, 2008).
- [4] Q. Lin, T. J. Johnson, R. Perahia, C. P. Michael, and O. J. Painter, *Opt. Express* **16**, 10596 (2008).
- [5] E. K. Tien, Y. W. Huang, S. M. Gao, Q. Song, F. Qian, S. K. Kalyoncu, and O. Boyraz, *Opt. Express* **18**, 21981 (2010).
- [6] M. R. E. Lamont, B. T. Kuhlmeier, and C. M. de Sterke, *Opt. Express* **16**, 7551 (2008).

CHAPTER 7

FUTURE DIRECTIONS

In Chapter 3, we have shown FWM-based wavelength conversion between the telecom and MIR regions in silicon nanowaveguides, demonstrating a continuous bandwidth across 803 nm, from 1619 nm to 2422 nm. In Chapter 6, we discuss extending the wavelength range of such devices further to the MIR by replacing the SiO₂ cladding with Si₃N₄ and utilizing higher-order dispersion to create discrete wavelength bands that satisfy phase matching. In modeling the FWM process, we have made several simplifications typically used when considering relatively narrow bandwidths. In particular, the wavelength dependence of the nonlinear parameter γ has not been included [1, 2], nor have we included the effect of a limited spatial mode overlap of the different waveguide modes for the signal, pump, and idler. An additional consideration is the accuracy of the material properties of the Si₃N₄ cladding at MIR wavelengths. In this thesis, the refractive index of Si₃N₄ has been extrapolated from telecom wavelengths, and the linear absorption at longer wavelengths has been assumed to be identical to that near 2.2 μm . Characterizing the refractive index and absorption loss of Si₃N₄ at longer wavelengths would improve the accuracy of our model going forward, as we analyze wavelength conversion over much broader bandwidths.

Experimentally, one of the key challenges will be efficient coupling into and out of the nanowaveguide over a broad wavelength range. Current taper designs are optimized for a relatively narrow wavelength range, and the aspheric lenses used in free-space coupling introduce chromatic aberrations and dispersion. In addition, we have observed a spatial walk-off of the signal, pump, and idler at the nanowaveguide

output, becoming more significant at larger signal-idler detunings. This walk-off becomes an issue when detecting wavelength conversion using the FTIR, since alignment of all beams into the detector is difficult after propagation through the interferometer. Chalcogenide fibers designed for MIR wavelengths may be a suitable alternative for output coupling, since the distance of free-space propagation would be reduced, but the coupling efficiency between the fiber and nanowaveguide remains to be investigated.

In Chapter 4, we have shown octave-spanning SCG characterized by soliton fission in silicon nanowaveguides, with dispersive wave generation at 1.5 μm and 3.6 μm . Though we have performed numerical simulations resulting in continuous spectra over this range, we have been limited experimentally by the pump power from the OPO. Performing the experiment with higher pump powers would result in a smooth, continuous spectrum. Additionally, we have yet to theoretically or experimentally investigate the spectral coherence and stability of the generated SCG. Theoretically, the first-order coherence can be calculated from numerical simulation of independently generated pairs of SC spectra [3, 4]. Experimentally, the fluctuations in spectral phase across the SCG can be characterized by taking an interferometric measurement between successive supercontinuum generated from a train of pulses [5]. As the SCG process here is seeded by soliton fission as opposed to modulation instability, we expect the coherence to be relatively high [5].

In Chapter 5, we have presented an investigation of silicon microresonator-based optical parametric oscillation at telecom and MIR wavelengths. While our numerical simulation shows good agreement with experimental results [6], we have neglected SRS in our model. It has been shown that Raman frequency combs can be

generated by engineering the cavity free spectral range to overlap with the peak of the Raman gain 15.6 THz away from the pump [7]. Including SRS in our simulations would enable analysis of the interplay between parametric FWM gain and Raman gain, and facilitate the experimental realization of a silicon-based Raman frequency comb in the MIR. In Chapter 5, we have also designed and analyzed an air-clad, etchless silicon microresonator which would enable generation of an octave-spanning frequency comb without the need for complex *p-i-n* integration. The linear absorption and free-carrier lifetime have been assumed to be identical to that of the SiO₂-clad silicon devices, so these air-clad microresonators still need to be fabricated and characterized. In addition, several technical and experimental issues remain to be investigated, such as coupling between the bus waveguide and microresonator. The decreased evanescent field resulting from the larger core-cladding index contrast may reduce the coupling efficiency.

In summary, we have presented in this thesis theoretical analyses and experimental demonstrations of FWM and SCG in silicon nanowaveguides in the MIR wavelength range. In addition, we have presented numerical modeling of OFC generation in silicon microresonators at telecom and MIR wavelengths. We have focused on the SOI platform, while investigating SiO₂, Si₃N₄, and air as cladding materials. The work reported here is an original and significant contribution to the field of nonlinear optics and constitutes substantial progress towards the development of silicon photonics for MIR applications.

REFERENCES

- [1] Q. Lin, J. Zhang, G. Piredda, R. W. Boyd, P. M. Fauchet, and G. P. Agrawal, *Appl. Phys. Lett.* **91**, 3 (2007).
- [2] A. D. Bristow, N. Rotenberg, and H. M. van Driel, *Appl. Phys. Lett.* **90**, 3 (2007).
- [3] J. M. Dudley and S. Coen, *Opt. Lett.* **27**, 1180 (2002).
- [4] J. M. Dudley and S. Coen, *IEEE J. Sel. Topics Quant. Electron.* **8**, 651 (2002).
- [5] J. M. Dudley, G. Genty, and S. Coen, *Rev. Mod. Phys.* **78**, 1135 (2006).
- [6] A. G. Griffith, R. K. W. Lau, J. Cardenas, Y. Okawachi, A. Mohanty, R. Fain, Y. H. D. Lee, M. Yu, C. T. Phare, C. B. Poitras, A. L. Gaeta, and M. Lipson, [arXiv:1408.1039](https://arxiv.org/abs/1408.1039) (2014).
- [7] T. Hansson, D. Modotto, and S. Wabnitz, [arXiv:1409.3047](https://arxiv.org/abs/1409.3047) (2014).